Medler, K, Mazzali, PA, Teffs, J, Ashall, C, Anderson, JP, Arcavi, I, Benetti, S, Bostroem, KA, Burke, J, Cai, YZ, Charalampopoulos, P, Elias-Rosa, N, Ergon, M, Galbany, L, Gromadzki, M, Hiramatsu, D, Howell, DA, Inserra, C, Lundqvist, P, McCully, C, Müller-Bravo, T, Newsome, M, Nicholl, M, Gonzalez, EP, Paraskeva, E, Pastorello, A, Pellegrino, C, Pessi, PJ, Reguitti, A, Reynolds, TM, Roy, R, Terreran, G, Tomasella, L and Young, DR

SN 2020acat: an energetic fast rising Type IIb supernova

Monthly Notices of the ROYAL ASTRONOMICAL SOCIETY

MNRAS **513,** 5540–5558 (2022) https://doi.org/10.1093/mnras/stac1192
Advance Access publication 2022 May 5

SN 2020acat: an energetic fast rising Type IIb supernova

K. Medler [1★] P. A. Mazzali,[1,2] J. Teffs [1] C. Ashall [3] J. P. Anderson,[4] I. Arcavi,[5,6] S. Benetti [7] K. A. Bostroem [8] J. Burke,[9,10] Y.-Z. Cai,[11] P. Charalampopoulos,[12] N. Elias-Rosa,[7,13] M. Ergon,[14,15] L. Galbany [13,16] M. Gromadzki [17] D. Hiramatsu,[18,19] D. A. Howell,[9,10] C. Inserra [20] P. Lundqvist [14,15] C. McCully,[9,10] T. Müller-Bravo [13] M. Newsome,[9,10] M. Nicholl,[21] E. Padilla Gonzalez,[9,10] E. Paraskeva,[22,23] A. Pastorello,[7] C. Pellegrino,[9,10] P. J. Pessi,[24] A. Reguitti [7,25,26] T. M. Reynolds [27] R. Roy,[28] G. Terreran,[9,10] L. Tomasella [7] and D. R. Young[29]

Affiliations are listed at the end of the paper

Accepted 2022 April 25. Received 2022 April 25; in original form 2022 January 16

ABSTRACT

The ultraviolet (UV) and near-infrared (NIR) photometric and optical spectroscopic observations of SN 2020acat covering ∼250 d after explosion are presented here. Using the fast rising photometric observations, spanning from the UV to NIR wavelengths, a pseudo-bolometric light curve was constructed and compared to several other well-observed Type IIb supernovae (SNe IIb). SN 2020acat displayed a very short rise time reaching a peak luminosity of $\mathrm{Log}_{10}(L) = 42.49 \pm 0.17$ erg s^{-1} in only $\sim 14.6 \pm 0.3$ d. From modelling of the pseudo-bolometric light curve, we estimated a total mass of ^{56}Ni synthesized by SN 2020acat of $M_{\mathrm{Ni}} = 0.13 \pm 0.03$ M$_\odot$, with an ejecta mass of $M_{\mathrm{ej}} = 2.3 \pm 0.4$ M$_\odot$ and a kinetic energy of $E_{\mathrm{k}} = 1.2 \pm 0.3 \times 10^{51}$ erg. The optical spectra of SN 2020acat display hydrogen signatures well into the transitional period ($\gtrsim$ 100 d), between the photospheric and the nebular phases. The spectra also display a strong feature around 4900 Å that cannot be solely accounted for by the presence of the Fe II 5018 line. We suggest that the Fe II feature was augmented by He I 5016 and possibly by the presence of N II 5005. From both photometric and spectroscopic analysis, we inferred that the progenitor of SN 2020acat was an intermediate-mass compact star with an M_{ZAMS} of 15–20 M$_\odot$.

Key words: supernovae: general – supernovae: individual: SN 2020acat.

1 INTRODUCTION

Type IIb supernovae (SNe IIb) belong to a subcategory of stripped envelope (SE) core-collapse supernovae (CC-SNe) that result from the explosion of stars with a zero age main-sequence mass (ZAMS) of $M_{\mathrm{ZAMS}} > 8$ M$_\odot$ (Smartt 2009). Prior to core collapse, the progenitors of SE-SNe undergo the stripping of their outer envelope leaving either a thin hydrogen layer, an open helium layer or a bare CO core at the time of explosion. The mechanism that removes mass from the outer envelope is thought to be either mass transfer via interaction with a companion star within a binary system, likely during the common envelope phase (e.g. Podsiadlowski, Joss & Hsu 1992; Naiman et al. 2019), or through the ejection of the outer layer by strong stellar winds from high-metallicity stars during the Wolf–Rayet phase (e.g. Gräfener & Vink 2015). This presents multiple potential formation channels for SE-SNe, resulting from either a binary or a single star system. Yet in recent years it seems that the binary star stripping mechanism has become the favoured formation method for SE-SNe. The distribution of ejecta mass derived from modelling of SE-SNe light curves has also been found to lie outside the range of ejecta masses based on exploding single star models (Lyman et al. 2016; Prentice et al. 2019). It has been suggested that the stellar winds predicted for the single star formation channel would not be able to account for the current observed rate of SE-SNe (Smith et al. 2011). As well as requiring the strong stellar winds, the high initial mass needed for the single star formation channel is strongly disfavoured by the stellar initial mass function (Smith et al. 2011). Along with the problems of low number of high-mass stars, analysis of a galactic sample of high-mass stars suggest that at least ∼ 70 per cent of these stars exist in interacting binary systems (Sana et al. 2012), further decreasing the amount of high-mass stars available for the single star formation channel. The explodability of single stars has also been discussed in recent years, with many finding that models for the highest mass progenitors fail to fully explode as an SE-SNe, collapsing directly into a black hole with either a faint or non-existent transient (O'Connor & Ott 2011; Zapartas et al. 2021). All of which points in the direction that the majority of SE-SNe originate from binary systems, rather than from single high-mass progenitors.

The various classifications of SE-SNe arise from progenitor stars that have undergone drastically different degrees of stripping prior to collapse, and display a large variety of spectral signatures throughout their evolution. If all or the majority of hydrogen is removed from the outer envelope, an H-poor SN Ib/c will occur. As a consequence, SNe Ib/c lack any prominent hydrogen features within their spectral evolution, and are dominated by helium and heavier elements. However, if there remains a significant mass of hydrogen, between 0.001 and 0.5 M$_\odot$ (Yoon, Dessart & Clocchiatti

★ E-mail: k.medler@2019.ljmu.ac.uk

2017; Sravan, Marchant & Kalogera 2019), an SN IIb will occur. Recently, it has been suggested that the lower limit to the mass of hydrogen for SN IIb is higher than previously thought, with a lower limit of $M_{\rm H} \approx 0.033$ M$_\odot$ (Hachinger et al. 2012; Gilkis & Arcavi 2022). Due to the presence of a thin hydrogen shell prior to core collapse, SNe IIb display strong hydrogen features in their spectra during the photospheric phase, with the Hα and Hβ lines being the most prominent features during this phase, along with several strong helium lines. The hydrogen features in SNe IIb fade over time until the spectra become SN Ib-like (Filippenko 2000). During the post-peak evolution, helium features start to dominate the spectra until the event transitions into the nebular phase, when oxygen lines become the strongest features within the spectra, along with several iron-group elements. The first SNe to display the signatures of a progenitor that possessed a thin hydrogen shell prior to core-collapse were SN 1987K (Fransson & Chevalier 1989) and SN 1993J (Woosley et al. 1994), with the latter becoming the template for the SNe IIb classification.

SNe IIb have a similar bolometric light-curve shape to SNe Ib. Despite their similar shape, SNe IIb tend to have on average a lower peak luminosity implying that SNe IIb produce a lower amount of ^{56}Ni (Prentice et al. 2019). Several SNe IIb and SNe Ib display an initial very bright peak several days before the main ^{56}Ni powered peak. This initial luminous peak is thought to result from the shock breakout on the stellar surface. As such, the shock breakout phase of the bolometric light curve contains vital information on the compactness of the progenitor prior to core-collapse. Both the presence and lack of any observed shock-cooling phase, especially if the SN is caught very early, can provide details on the type of progenitor. This shock-cooling tail was seen in SN 1993J (Wheeler et al. 1993), SN 2008D (Malesani et al. 2009), SN 2011fu (Morales-Garoffolo et al. 2015), SN 2013df (Morales-Garoffolo et al. 2014), and SN 2016gkg (Bersten et al. 2018), although not all SE-SNe display evidence of this shock-cooling tail such as with SN 2008ax (Roming et al. 2009).

In this paper, we present the ultraviolet (UV), optical, and near-infrared (NIR) observations of the SN IIb 2020acat. Photometric coverage includes UV–NIR observations, while the spectra cover the optical observations. In Section 2, we discuss the distance and reddening associated with the host galaxy of SN 2020acat, along with the explosion date. In Section 3, we present the acquisition of the UV–NIR photometric data and the spectral evolution of SN 2020acat. In Section 4, we discuss evolution of the *UV* − *NIR* photometric bands, along with the fast rising pseudo-bolometric light curve and the derived physical parameters of SN 2020acat, as well as comparisons with other SNe IIb. Then, in Section 5, we examine the spectroscopic evolution of SN 2020acat within the photospheric, transitional, and early nebular phases, including the line velocity of the Hα, Hβ, He I 5867, and Fe II 5018. We also compare the optical spectra of SN 2020acat with those of other well-observed SNe IIb. We then analyse the late time spectra and place constraints on the mass of oxygen synthesized by SN 2020acat. Finally, in Section 6, we summarize our analysis of SN 2020acat.

2 HOST GALAXY AND EXPLOSION DATE

SN 2020acat was discovered in the galaxy PGC037027 (Srivastav et al. 2020), a $W1 = 14.50 \pm 0.03$ mag galaxy (Cutri et al. 2013), at a redshift of $z = 0.007\,932 \pm 0.000\,150$. SN 2020acat was located 26.70 arcsec south and 19.90 arcsec west of the Galactic Centre, at a projected distance of ∼5.7 kpc. Fig. 1 shows the location of SN 2020acat and the surrounding stars that were

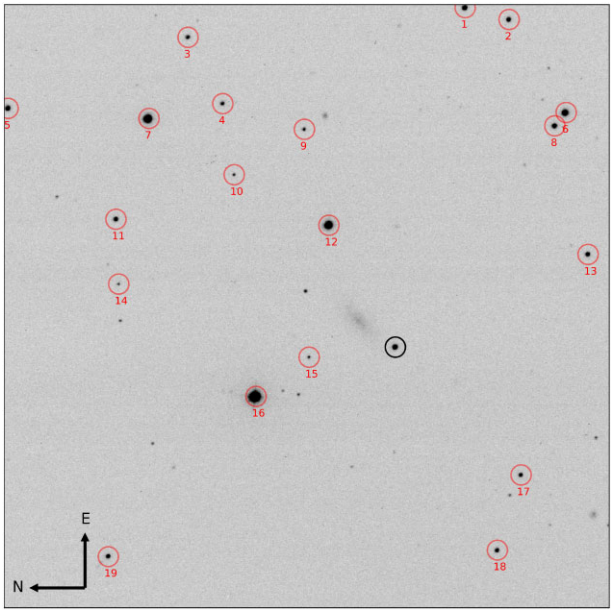

Figure 1. *ugriz* combined image of SN 2020acat (black) and surrounding standard stars (red), taken on December 22, 2020 during peak light using the Liverpool Telescope. The standard stars were used to calibrate the LT *ugriz* photometry.

used for photometric calibration. Using the NASA/IPAC Extragalactic Database (NED[1]) default cosmology of $H_0 = 73.0 \pm 5$ kms^{-1}Mpc^{-1}, $\Omega_{\rm matter} = 0.27$, and $\Omega_{\rm vacc} = 0.73$ (Spergel et al. 2007), the host galaxy distance was found to be 35.3 ± 4.4 Mpc, derived from the model based on the local velocity field given in Mould et al. (2000) using the terms for the influence of the Virgo Cluster, the Great Attractor, and the Shapley Supercluster. The error associated with the distance modulus accounts for the error from the velocity field correction. An additional uncertainty on the distance is included relating to the low redshift of SN 2020acat, placing the host galaxy outside the Hubble flow regime. This uncertainty is of the order of 10 per cent for SN 2020acat that arises from the peculiar velocity of the host galaxy and has been added in quadrature to the distance error. From the host galaxy distance, the implied distance modulus for SN 2020acat is $m - M = 32.74 \pm 0.27$ mag.

The line of sight dust extinction of the host galaxy, $E(B-V)_{\rm host}$, associated with SN 2020acat, is expected to be negligible. No strong, narrow interstellar Na ID lines were detected at the redshift of the host galaxy; see Section 5. This lack of strong Na I D lines, along with the position of SN 2020acat relative to its host galaxy, implies that $E(B-V)_{\rm host}$ is negligible. The Milky Way (MW) extinction, $E(B-V)_{\rm MW}$, takes a value of $E(B-V)_{\rm MW} = 0.0207 \pm 0.0004$ mag, derived from the Schlafly & Finkbeiner (2011) dust map. Thus, we assume a total extinction for SN 2020acat to be $E(B-V)_{\rm tot} = 0.0207 \pm 0.0004$ mag.

The first detection of SN 2020acat, taken on MJD = 59192.65 (December 9, 2020), occurred almost exactly 2 d after that last non-detection taken by the Asteroid Terrestrial-impact Last Alert System (ATLAS; Tonry et al. 2018; Smith et al. 2020) on MJD = 59190.61 (December 7, 2020). This last non-detection had a limiting magnitude of 19.33 mag in the ATLAS *o*-band, approximately ∼0.78 mag dimmer than the initial observation. The last non-detection places a

[1]https://ned.ipac.caltech.edu/.

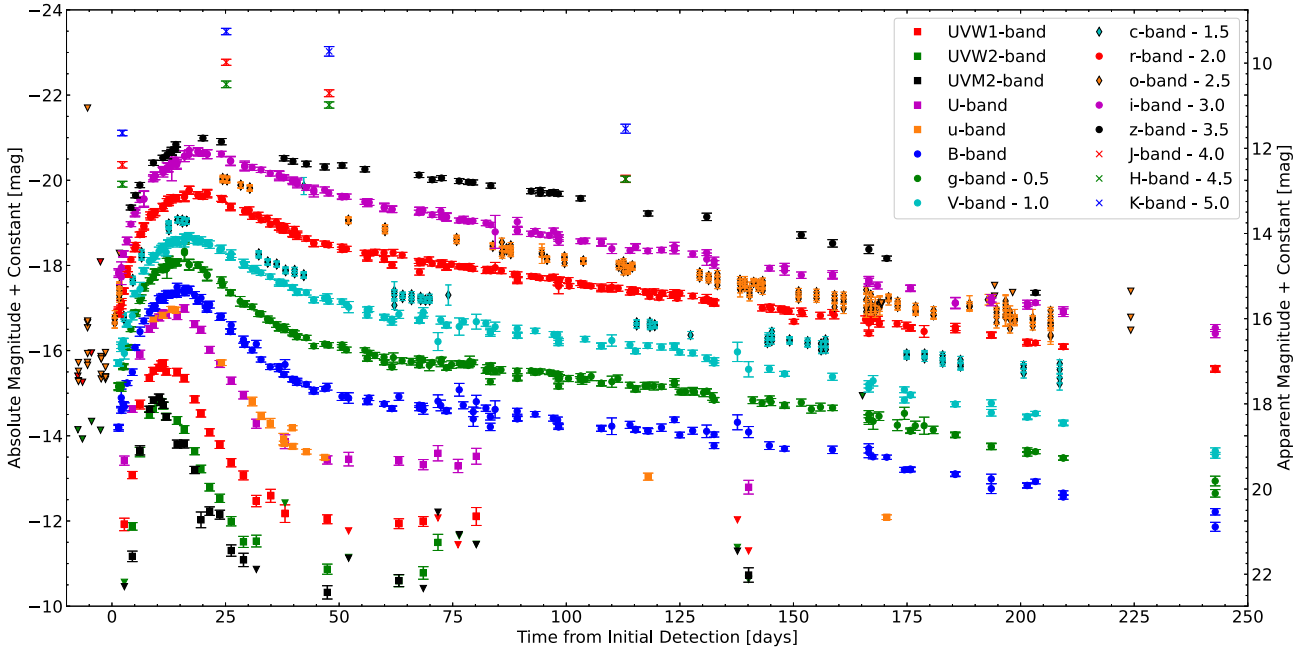

Figure 2. UV–NIR photometric observations of SN 2020acat, with phase relative to explosion date (MJD = 59192.01) and given in the rest frame. Each photometric band is given a marker signifying its location on the electromagnetic spectrum; UV = square, optical = circle, and NIR = crosses. All photometric band limits are given by the solid triangles, with optical band limits having black outlines. Additionally, the ATLAS bands are given by the coloured diamonds with the black outline and are separate from the other optical bands due to the broad nature of the ATLAS filters.

strong constraint on the explosion date and suggests that SN 2020acat was caught very early. From fitting the pseudo-bolometric light curve (see Section 4.3), an explosion date of MJD = 59192.01 ± 0.14 was determined. This estimate is taken as the explosion date throughout this work.

3 DATA ACQUISITION

3.1 Photometry

Photometry of SN 2020acat was obtained in the UV (*UVW*2, *UVM*2, *UVW*1, *u*, *U*), optical (*BgVriz*), and NIR (*JHK*) photometric bands, displayed in Fig. 2 along with the ATLAS *c* + *o* bands. SN 2020acat was initially detected by ATLAS on MJD = 59192.65 (December 9, 2020), and followed in the ATLAS *c* + *o* bands for ∼210 d. Additional optical follow-up of SN 2020acat in the *BgVriz* bands was obtained from several telescopes over the campaign lasting ∼230 d. These telescopes include the 2.0-m Liverpool Telescope (LT; Steele et al. 2004), the 2.56-m Nordic Optical Telescope with the Alhambra Faint Object Spectrograph and Camera (ALFOSC) and the 1.82-m Copernico Asiago Telescope (CT) with AFOSC. Additional photometry was provided by the Palomar 1.2-m Samuel Oschin telescope using the Zwicky Transient Facility camera (ZTF-cam; Bellm et al. 2018), the 67/92-cm Schmidt telescope at the Cima Ekar Observing Station and several telescopes as part of the Las Cumbres Observatory (Las Cumbres; Brown et al. 2013) through the Global Supernova Project (GSP; Howell 2019). All data reduction was done by automatic pipelines associated with each telescope group, with photometric magnitudes obtained through point spread function (PSF) photometry. UV photometry of SN2020acat was obtained by the Neil Gehrels *Swift* Observatory (*Swift*; Roming et al. 2005) between December 11, 2020 and April 28, 2021. The UVOT data were reduced using the standard pipeline available in the HEASOFT software package[2] using the latest version of CALDB. Observation of every epoch was conducted using one or several orbits. To improve the signal-to-noise ratio (S/N) of the observation in a given band in a particular epoch, all orbit-dates were co-added for that corresponding epoch using the HEASOFT routine `uvotimsum`. The routine `uvotdetect` was also used to determine the correct position of the transient (which is consistent with the ground-based optical observations) and used the routine `uvotsource` to measure the apparent magnitude of SN 2020acat by performing aperture photometry. For source extraction, a small aperture of radius 3.5 arcsec was used, while an aperture of radius 100 arcsec have been used to determine the background. The SN is located at the outskirts of its host, implying a negligible host contribution in the *NUV* bands. Moreover, as a small aperture has been used to extract the flux at the SN location, considerable host contribution is also not expected in the *Swift* optical ('U,B,V') bands. The NIR photometry was obtained by the 2.56-m Nordic Optical Telescope (NOT; Djupvik & Andersen 2010) equipped with NOTCAM through the NOT Unbiased Transient Survey 2 (NUTS2) and the 3.58-m New Technology Telescope (NTT; Wilson 1983) through the ESO Spectroscopic Survey for Transient Objects (ePESSTO +; Smartt et al. 2015) with SOFI (Moorwood, Cuby & Lidman 1998). All photometry have been corrected for reddening, although host galaxy image subtractions were not performed. The host galaxy of SN 2020acat lacked UV and optical observations prior to SN 2020acat making host subtraction not possible until after SN 2020acat has fully faded. However, this lack of host galaxy subtractions is not expected to affect the photometry of SN 2020acat due to its distance from galactic centre.

[2] https://heasarc.nasa.gov/lheasoft/.

3.2 Spectroscopy

SN 2020acat was classified as an SN IIb on MJD = 59193.31 (December 10, 2020; Pessi et al. 2020) using the spectrum obtained by ePESSTO + using the ESO Faint Object Spectrograph and Camera (EFOSC2; Buzzoni et al. 1984) mounted on the NTT. The classification spectrum was obtained ∼1.3 d after the explosion. Further optical spectroscopic observations of SN 2020acat were obtained from ePESSTO+ using EFOSC2 with the NTT. Spectroscopic observations from ePESSTO + were obtained with the blue grism, gr11 (3380–7520 Å), and the red grism, gr16 (6015–10 320 Å). These EFOSC2 spectra were combined to form a single spectrum at each epoch with full optical coverage. Several additional spectra were obtained during the evolution of SN 2020acat using the Spectrograph for the Rapid Acquisition of Transients (SPRAT; Piascik et al. 2014) mounted on the LT, the Supernova Integral Field Spectrograph (SNIFS; Lantz et al. 2004) camera mounted on the Hawaii-based UH88 telescope and via the NUTS2 programme using the ALFOSC mounted on NOT using grism 4. Further spectra were obtained through Las Cumbres using the FLOYDS spectrographs mounted on the 2 m Faulkes Telescope South (FTS) and the 2-m Faulkes Telescope North (FTN), based at the Siding Spring Observatory (COJ) and the Haleakala Observatory (OGG), respectively. Spectra were also obtained using the 1.82-m Copernico telescope using AFOSC, with both the VPH7 and VPH6 grisms. All spectra were reduced in the standard procedure for each telescope. The spectroscopic follow-up campaign lasted for ∼230 d before SN 2020acat was no longer observable. The spectroscopic evolution of SN 2020acat is shown in Fig. 3, with the details on the spectroscopic observations given in Table 1.

4 PHOTOMETRY ANALYSIS

4.1 UV–NIR light curves

The *UV* bands of SN 2020acat were only followed for ∼135 d before becoming too dim to observe. While the optical bands were followed for a total of ∼250 d, with the *NIR* bands being observed a few times throughout the follow-up campaign. The rise of the UV and optical light curves was observed with a fast cadence. The close proximity of initial observation and the last non-detection, along with the depth of the limit in the ATLAS *o* band, argues against the possibility of a long-duration shock-cooling phase occurring prior to the observe rise, such as those seen in SN 1993J (Lewis et al. 1994), SN 2011dh (Arcavi et al. 2011) or SN 2016gkg (Arcavi et al. 2017). The lack of a long duration shock-cooling tail was also confirmed by the *UV* bands, which commonly show the cooling tail if it is indeed present. The *UV* bands of SN 2020acat, first observed ∼2.5 d after the estimated explosion date, lack any deviation from the fast rise seen in the other redder bands, strongly implying a lack an extended shock-cooling tail.

The peaks of all but the *NIR* bands were well observed, allowing constraints to be placed on the epoch of maximum brightness and the value for peak magnitude in each band. The epoch of peak brightness in each band, $t_{\rm peak}$, along with the rise time, peak apparent and absolute magnitudes are given in Table 2. The values of $t_{\rm peak}$ were determined by fitting a cubic spline to the each bands light curves around peak time. The error associated with the peak time is a combination of the error from the explosion date and the fitting of the cube spline. Unfortunately, the reduced number of observations in the *z* band around maximum light resulted in the value of $t_{\rm peak}$ having a greater error than the other bands. It should be noted that, due to the lack of any *JHK*-band data around peak time, a spline could not be fitted without placing an extremely large uncertainty to the epochs of maximum light.

SN 2020acat has an incredibly fast rise time for an SNe IIb, with the *UV* bands peaking in ∼10 d, while the optical bands peaking in ∼14–22 d. This is faster than the average SNe IIb that reaches a peak in the *UV* bands in $\gtrsim$ 15 d, with the optical bands reach peak in $\gtrsim$ 20 d, as seen with SN 2008ax (Roming et al. 2009) and SN 2011dh (Marion et al. 2014). The *UV* bands also display a very fast decline once they reach peak light, with an average decline in magnitude over the first 15 d from peak brightness, Δm_{15}, of $\Delta m_{15}^{UV} = 2.35 \pm 0.04$ mag. While the average Δm_{15} for the optical bands was $\Delta m_{15}^{opt} = 0.77 \pm 0.24$ mag, suggesting that the ejecta of SN 2020acat rapidly expanded and cooled scattering the light to lower energy bands. When compared to the Δm_{15} of 10 SNe IIb, with an average optical band decline of $\Delta m_{15}^{opt} = 0.92 \pm 0.22$ mag (Taddia et al. 2018), SN 2020acat declined in brightness at a slightly slower rate remaining brighter for longer. The *B* band of SN 2020acat had a rise time of $B_{t_{\rm r}} = 15.18 \pm 0.75$ d, roughly 4 d faster than for SN 1993J ($B_{t_{\rm r}} = 18.97$ d; Richmond et al. 1994), SN 2008ax ($B_{t_{\rm r}} = 18.9$ d; Pastorello et al. 2008), SN 2011dh ($B_{t_{\rm r}} = 19.6$ d; Sahu, Anupama & Chakradhari 2013), and SN 2011fu ($B_{t_{\rm r}} = 23.23$ d; Kumar et al. 2013). Interestingly, the *B*-band rise time of SN 2020acat lies between the $B_{t_{\rm r}}$ values of SNe II ($B_{t_{\rm r}} = 8.3 \pm 2.0$ d) and SNe IIb ($B_{t_{\rm r}} = 19.0 \pm 1.8$ d) found by Pessi et al. (2019), suggesting that SN 2020acat was an outlier in the hydrogen-rich SE-SNe group and may have been a transitional event between the standard SNe II and SNe IIb. The short rise time also places a strong constraint on the existence of any possible shock-cooling tail, a feature associated with progenitors that lack an extended radii, as was seen with hydrodynamical models (Bersten et al. 2012).

4.2 Colour evolution

The $(UVW2 - V)$, $(UVM2 - V)$, $(UVW1 - V)$, $(U - B)$, $(B - V)$, $(g - r)$ $(r - i)$, and $(i - z)$ colours of SN 2020acat are given in Fig. 4. For the $(U - B)$ evolution, additional data were added using the $(u - g)$ and $(B - V)$ colours that form a relation with $(U - B)$, as given by Jordi, Grebel & Ammon (2006), of

$$(U - B) = \frac{(u - g) - (0.770 \pm 0.05)(B - V) - (0.72 \pm 0.04)}{(0.75 \pm 0.05)}. \quad (1)$$

It should be noted that equation (1) makes use of stellar colours to determine the relation parameters between the *U*- and *B*-bands. However, when the colours derived from equation (1) were compared to the values of $(U - B)$ obtained from photometry there was little appreciable difference between the derived colour evolutions.

The colours obtained from the UV and optical photometry of SN 2020acat were all fit with a combination of a Gaussian function, to follow the initial decline and rise seen within the first few weeks, and a linear decay function, which fits to the late time colour decline and assumes a constant decline after the initial red peak around day ∼35. The evolution function is shown as a solid black line in Fig. 4. Other SNe were not fit with the evolution function as they either did not follow the initial decline seen in SN 2020acat or lacked enough photometric data to fit the evolution function.

Initially, the colours of SN 2020acat start relatively red and rapidly become bluer within the first two weeks, reaching minima at around day ∼10–15. After this blue minima, the colours evolve redward until they peak at ∼35–45 d. The fast reddening seen during the weeks after the blue minima results from the cooling of the expanding ejecta and the shift in the peak of the blackbody emission to the redder

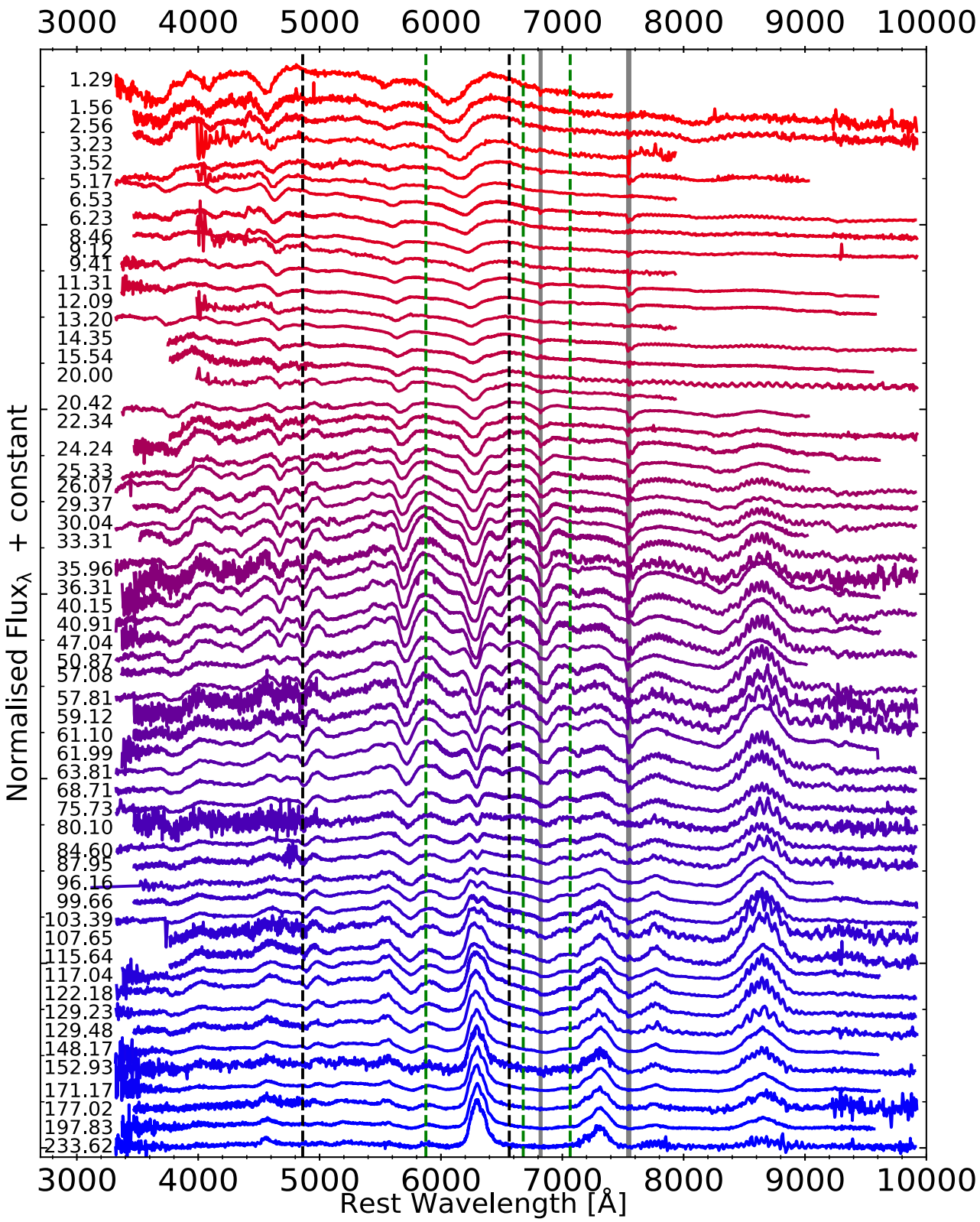

Figure 3. Spectroscopic evolution of SN 2020acat. Flux is normalized to the Hα feature or the peak of the O I $\lambda\lambda$6300, 6363 feature depending on what was stronger at the time of observation. See Table 1 for the details on each spectrum. The phase of spectra is given on the left-hand side. Both the hydrogen (black) and main optical helium (green) lines are given by the dashed lines at their rest wavelength, along with the telluric features that are denoted by the grey regions.

Table 1. Information on spectroscopic follow-up campaign for SN 2020acat.

Spectrum	Epoch (d)	Observation date (UT)	Telescope[a]	Range (Å)
1	1.29	07:21:47 10/12/20	NTT	3323–7406
2	1.56	13:56:22 10/12/20	LasC$_\alpha$	3470–9921
3	2.56	14:13:23 11/12/20	LasC$_\alpha$	3470–9922
4	3.23	06:20:02 12/12/20	LT	3988–7931
5	3.52	13:23:36 12/12/20	UH88	3376–9028
6	5.17	05:20:31 14/12/20	LT	3988–7931
7	6.23	06:59:30 15/12/20	NTT	3323–9910
8	6.53	14:12:06 15/12/20	LasC$_\alpha$	3471–9921
9	8.46	12:54:15 17/12/20	LasC$_\alpha$	3470–9921
10	9.12	04:51:08 18/12/20	LT	3988–7931
11	9.41	11:53:10 18/12/20	NOT	3370–9600
12	11.31	09:51:05 20/12/20	NOT	3371–9580
13	12.09	04:47:46 21/12/20	LT	3988–7931
14	13.20	07:34:23 22/12/20	NTT	3323–9910
15	14.35	11:25:59 23/12/20	NOT	3751–9556
16	15.54	16:06:27 24/12/20	LasC$_\beta$	3769–9922
17	20.00	03:57:18 29/12/20	LT	3988–7931
18	20.42	14:18:10 29/12/20	UH88	3376–9028
19	22.33	12:35:17 31/12/20	LasC$_\alpha$	3767–9922
20	24.24	10:30:45 02/01/21	NOT	3473–9612
21	25.33	12:54:04 03/01/21	UH88	3376–9028
22	26.07	06:54:28 04/01/21	NTT	3323–9910
23	29.38	14:46:34 07/01/21	LasC$_\alpha$	3471–9921
24	30.04	06:56:26 08/01/21	NTT	3323–9910
25	33.31	13:54:24 11/01/21	UH88	3518–9019
26	35.96	06:05:24 14/01/21	NTT	3323–9910
27	36.31	14:31:12 14/01/21	LasC$_\beta$	3471–9922
28	40.15	11:34:23 18/01/21	ASI	3374–9610
29	40.91	05:54:07 19/01/21	NTT	3323–9910
30	47.04	10:09:25 25/01/21	NOT	3372–9615
31	50.87	06:53:36 29/01/21	NTT	3325–9911
32	57.08	12:59:24 04/02/21	UH88	3369–9010
33	57.81	06:40:43 05/02/21	NTT	3325–9912
34	59.12	14:29:24 06/02/21	LasC$_\beta$	3471–9921
35	61.10	14:11:41 08/02/21	LasC$_\beta$	3469–9922
36	61.99	11:50:35 09/02/21	NOT	3371–9601
37	63.81	07:52:36 11/02/21	NTT	3325–9911
38	68.71	06:16:37 16/02/21	NTT	3323–9910
39	75.73	08:17:39 23/02/21	NTT	3327–9911
40	80.09	17:49:21 27/02/21	LasC$_\beta$	3470–9921
41	84.60	06:41:28 04/03/21	NTT	3331–9911
42	87.95	15:46:53 07/03/21	LasC$_\beta$	3471–9920
43	96.16	10:15:06 16/03/21	ASI	3124–9224
44	99.66	11:03:20 19/03/21	LasC$_\alpha$	3470–9921
45	103.39	05:12:08 23/03/21	NTT	3327–9911
46	107.65	12:14:05 27/03/21	LasC$_\beta$	3767–9922
47	115.64	13:37:24 04/04/21	LasC$_\beta$	3768–9922
48	117.04	23:23:00 05/04/21	NOT	3376–9611
49	122.18	03:45:14 11/04/21	NTT	3327–9911
50	129.23	06:23:16 18/04/21	NTT	3323–9910
51	129.48	12:24:11 18/04/21	LasC$_\beta$	3470–9922
52	148.17	08:26:10 07/05/21	NOT	3370–9600
53	152.93	03:40:55 12/05/21	NTT	3318–9904
54	171.17	12:54:07 30/05/21	NOT	3373–9611
55	177.03	10:27:00 05/06/21	LasC$_\beta$	3471–9922
56	197.83	09:42:37 26/06/21	NOT	3373–9569
57	233.62	11:30:24 01/08/21	NTT	3319–9910

Notes. The epochs are relative to the explosion date (MJD = 59192.01) and are given in the rest frame. Wavelength range is also given in the rest frame. [a]Telescope and instrument; 1. NTT = NTT using EFOSC2; 2. LasC = α: FTS using FLOYDS, β: FTN using FLOYDS; 3. LT = LT using SPRAT; 4. NOT = NOT using ALFOSC; 5. UH88 = UH88 using SNIFS; 6. ASI = CT using AFOSC.

Table 2. Peak time, rise times, and both apparent and absolute peak magnitudes for the UV–optical photometry bands for SN 2020acat.

Band	t_{peak} (MJD)	Rise time (t_r) (d)	m_{peak} (mag)	M_{peak} (mag)
UVW2	59202.20 ± 0.64	10.19 ± 0.40	18.20 ± 0.03	−14.72 ± 0.05
UVM2	59202.36 ± 0.64	10.35 ± 0.40	18.09 ± 0.04	−14.84 ± 0.05
UVW1	59203.54 ± 0.66	11.53 ± 0.42	17.32 ± 0.03	−15.64 ± 0.06
u	59204.77 ± 0.47	12.76 ± 0.20	15.89 ± 0.02	−16.95 ± 0.04
U	59204.88 ± 0.66	12.87 ± 0.41	15.83 ± 0.02	−17.01 ± 0.06
B	59207.19 ± 0.88	15.18 ± 0.75	15.42 ± 0.04	−17.40 ± 0.11
g	59208.06 ± 0.92	16.05 ± 0.82	15.16 ± 0.01	−17.65 ± 0.12
V	59208.65 ± 0.85	16.64 ± 0.71	15.18 ± 0.01	−17.62 ± 0.11
r	59210.20 ± 0.88	18.19 ± 0.75	15.09 ± 0.01	−17.70 ± 0.12
i	59212.17 ± 1.10	20.16 ± 1.18	15.14 ± 0.01	−17.64 ± 0.11
z	59213.09 ± 1.53	21.08 ± 2.29	15.23 ± 0.05	−17.44 ± 0.05

Notes. The rise times are given in the rest frame. The *NIR* bands (*JHK*) have insufficient data around peak and are excluded.

bands. The reddening is also a result of line blanketing brought about by iron-group elements within the inner ejecta. Once the red peak is reached, all colours slowly decline over the next ∼135 d. This decline is expected as the ejecta became optically thin after ∼40 d allowing for trapped photons to escape the inner ejecta. The $(U - B)$ colour declines at a much faster rate, ∼0.007 mag d^{-1}, compared to the other colours, with the $(B - V)$, $(g - r)$, and $(r - i)$ having a decline of ∼0.004, ∼0.002, and ∼0.003 mag per day, respectively. While the $(U - B)$ and $(B - V)$ colours follow a smooth decline at the late time ($t > 150$ d), both the $(g - r)$ and $(r - i)$ colours diverge from a linear decline. The $(g - r)$ colour starts to rapidly grow redder, while the $(r - i)$ colour evolution seems to rise at a slower pace. At this time, the effect of blackbody radiation has fully faded from the colour evolution and the reddening effect seen in both the $(g - r)$ and $(r - i)$ colours is likely brought about by the emergence of the oxygen λλ6300, 6363 and calcium λλ7292, 7324 lines that dominate the spectra at this epoch. These emission lines roughly correspond to the central wavelengths of the *r*- and *i*-bands and dominate the contribution to the total flux in each band, thus drastically increasing the strength of these bands relative to the other photometric bands.

The multiband colour evolution of SN 2020acat is compared to those of SN 1993J (Richmond et al. 1994, 1996; Barbon et al. 1995), SN 2008ax (Pastorello et al. 2008; Tsvetkov et al. 2009; Taubenberger et al. 2011), SN 2011dh (Tsvetkov et al. 2012; Sahu et al. 2013; Brown et al. 2014; Ergon et al. 2014), and SN 2016gkg (Brown et al. 2014; Arcavi et al. 2017; Bersten et al. 2018). These SNe IIb were chosen as comparison objects for SN 2020acat as they all possess comprehensive photometric and spectroscopic data around peak time, as well as into the late time when the hydrogen features have faded. The thoroughly documented nature of these events mean they have well-known properties, allowing a comprehensive comparison between the results obtained from the Arnett-like model described below and the literature values. This is used as a test to validate the model used and thus the results obtained for SN 2020acat. The colour evolutions of these SNe IIb are also given in Fig. 4, with details on each SN IIb given in Table 3. For several SNe, only Johnson–Cousins photometric bands were available for the redder $(r - i)$ bands, such as SN 1993J. For these SNe, a conversion to Sloan Digital Sky Survey (SDSS) red bands was done using equation (2) and (3) also from Jordi et al. (2006):

$$(g - r) = (1.646 \pm 0.008)(V - R) - (0.139 \pm 0.004) \quad (2)$$

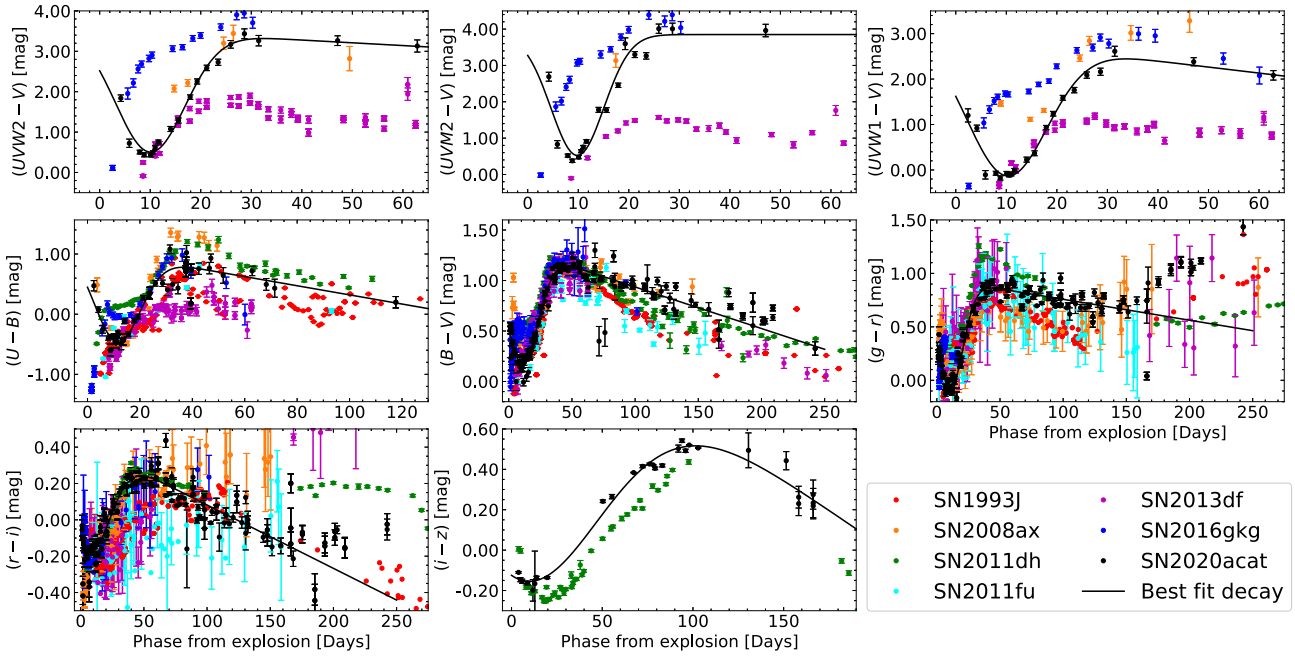

Figure 4. The $(UVW2 - V)$, $(UVM2 - V)$, $(UVW1 - V)$, $(U - B)$, $(B - V)$, $(g - r)$, $(r - i)$, and $(i - z)$ colours of SN 2020acat (black) compared to the colours of SN 1993J (red), SN 2008ax (orange), SN 2011dh (green), SN 2011fu (cyan), SN 2013df (magenta), SN 2016gkg (blue). The colours of SN 2020acat were fit with a decay function (black line) that assumes a linear decline at late times, $\gtrsim$ 35–45 d. All SNe colours are given in the rest frame.

Table 3. Details for the SNe IIb that are compared with SN 2020acat.

SN	Explosion date (MJD)	Redshift	Distance (Mpc)	$E(B-V)_{MW}$ (mag)	$E(B-V)_{Host}$ (mag)	Source
1993J	49072.0	−0.001 13	2.9	0.069	0.11	1,2,3
2008ax	54528.8	0.004 56	20.25	0.022	0.278	4,5
2011dh	55712.5	0.001 638	7.80	0.035	0.05	6,7,9
2011fu	55824.5	0.001 845	74.5	0.068	0.035	8
2013df	56447.8	0.002 39	21.4	0.017	0.081	10,11
2016gkg	57651.2	0.0049	21.8	0.0166	0.09	12,13
2020acat	59192.01	0.007 932	35.32	0.0207	–	–

Notes. 1. Richmond et al. (1994), 2. Barbon et al. (1995), 3. Richmond et al. (1996), 4. Pastorello et al. (2008), 5. Tsvetkov et al. (2009) 6. Tsvetkov et al. (2012), 7. Sahu et al. (2013), 8. Kumar et al. (2013), 9. Brown et al. (2014), 10. Morales-Garoffolo et al. (2014), 11. Dyk et al. (2014), 12. Arcavi et al. (2017), 13. Bersten et al. (2018).

and

$$(r - i) = (1.007 \pm 0.005)(R - I) - (0.236 \pm 0.003). \quad (3)$$

As with equation (1), it should be noted that the colours derived from equation (2) and equation (3) make use of stellar colours and should be taken as a way of obtaining the trend of colour evolution's for SNe that lack SDSS photometric bands.

While a comprehensive comparison of the colour evolution's of SN 2020acat can be done with the majority of the optical bands, the same cannot be said for the UV colours and the $(i - z)$ evolution. This is due to the lack of *UV*- and *z*-band data for several of these SNe. The colour evolution of SN 2020acat initially follows the same trend as SN 2008ax, displaying an initial decline to a bluer colour before rising to a red peak within approximately four weeks of the explosion. This is expected for SNe that lack detection of a strong shock-cooling tail that is shown as an initial very blue colour before becoming redder, such as SN 1993J. After the red maximum at approximately four weeks post-explosion, the colours of SN 2020acat follow the shape of SN 1993J and SN 2011dh, which both display a decline for several months before changing slope, although the rate of decline of SN 2020acat is much slower than the other SNe. At around ∼140–150 d after explosion several SNe, including SN 2020acat, diverge from a linear decay in the $(g - r)$ and $(r - i)$ bands. The $(g - r)$ colour of SN 2008ax also displays this increase, although the rise is at a much slower pace compared to both SN 1993J and SN 2020acat. The $(r - i)$ colour evolution of SN 2020acat is quite similar to both SN 1993J and SN2011fu in the decline phase. Interestingly, the shape of the $(i - z)$ colour evolution of SN 2020acat is very similar to that of SN 2011dh, despite the clear differences seen in the bluer colours. Although the overall $(i - z)$ colour of SN 2020acat is redder than that of SN 2011dh and reaches the blue minima ∼10 d before SN 2011dh.

4.3 Bolometric light curve

A pseudo-bolometric light curve was constructed using the *UV* – *NIR* photometric bands in order to obtain the physical parameters of SN 2020acat. The pseudo-bolometric light curve was constructed by integrating the flux of the *UV* – *NIR* bands and applying a blackbody correction. During epochs where *NIR* bands are missing, the magnitude is obtained by interpolating the points using a polynomial fit. Blackbody corrections were calculated by fitting the available spectral energy distribution (SED) with a blackbody function and extrapolating out to the extremes of the UV and NIR regions when necessary. The error associated with the pseudo-bolometric light curve was calculated using the error for the individual photometry points, along with an error calculated from the fitting of the extrapolated SED and an additional error of 0.1 mag per 10 d applied to the extrapolated photometry bands. Further errors for the *UV*-band extrapolations were added in quadrature to the total luminosity error.

Additional pseudo-bolometric light curves were constructed using the UV – optical, solely optical, and optical – NIR photometry. These pseudo-bolometric light curves are presented in the top panel of Fig. 5, while the contribution of each electromagnetic region to

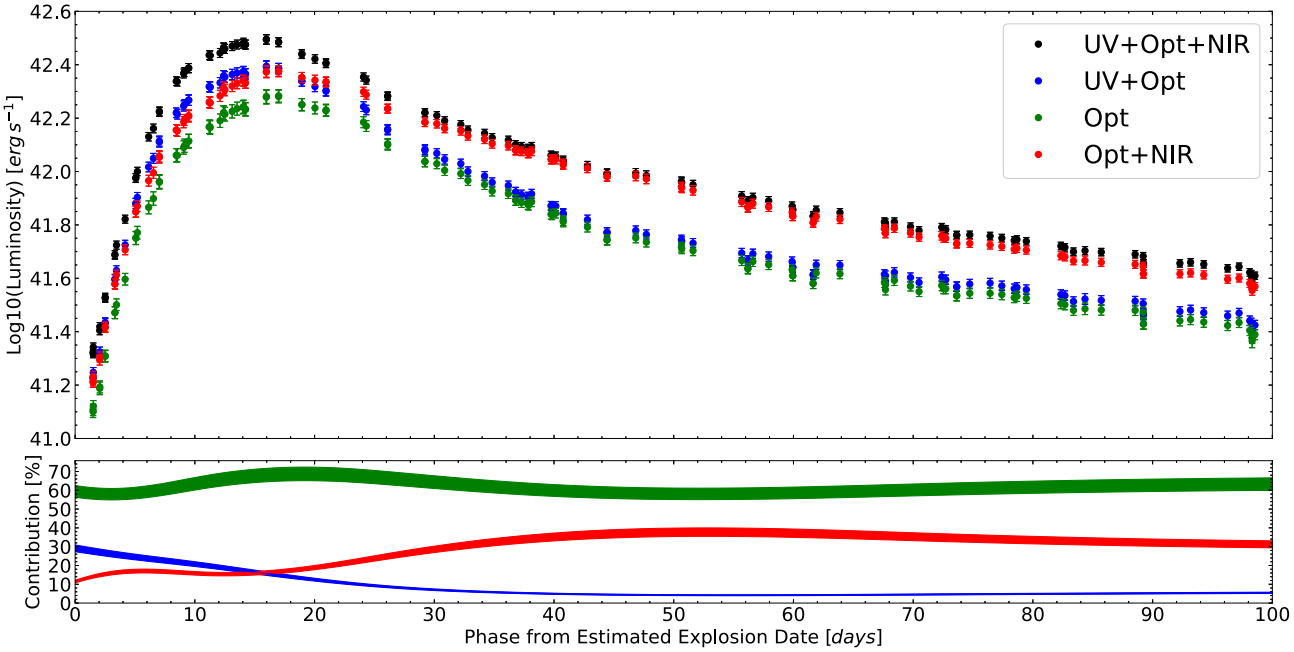

Figure 5. Top panel: the pseudo-bolometric light curve of SN 2020acat, along with the light curves constructed using the UV + optical, just optical, and optical + NIR photometry. Bottom panel: the contribution of the individual electromagnetic regions as a percentage of the pseudo-bolometric light curve, with UV = blue, Optical = green, and NIR = red.

the complete pseudo-bolometric light curve given can be seen in the lower panel of Fig. 5. The optical bands contribute the most to the total light curve throughout its evolution. Initially, the *UV* bands dominate over the *NIR* bands, before rapidly decline in strength as the NIR contribution increases, peaking at around ∼35 per cent and staying relatively constant until $\gtrsim$ 150 d, when the NIR contribution rises. The contribution from the NIR photometry bands shown in Fig. 5 is initially slightly inflated due to the interpolation at early times resulting in an overestimation in the strength of the *NIR* bands. This lack of comprehensive photometric coverage for the NIR region resulted in an increase in the final error for the pseudo-bolometric light curve. However, the lack of NIR coverage at peak time is not expected to have a significant effect on the physical parameters derived from the pseudo-bolometric light curve due to the domination of the *UV* and optical bands at this epoch. The error of the pseudo-bolometric light curve was also influenced by the lack of *UV* bands at late times ($\gtrsim$ 60 d), although at this epoch the *UV* bands contribute little to the bolometric light curve ($\lesssim$10 per cent of total flux), and therefore is not expected to impose significant errors. The late time pseudo-bolometric light curve of SN 2020acat is likely suffers from an overestimation of the *NIR* bands during the period when they contribute significantly to the total light curve. While the pseudo-bolometric light curve constructed from the *UV* − *NIR* bands encapsulates the majority of photons emitted during the evolution of SN 2020acat, a small portion of light is unaccounted for associated with the bands outside the observed wavelength range. A full bolometric light curve of SN 2020acat is expected to have a slightly higher peak luminosity and more luminous late time due to the domination of the infrared bands during this epoch, as seen in Fig. 5. Fitting of the full bolometric light curve during the photospheric phase would result in a slightly larger ^{56}Ni mass, and potentially a higher amount of ejecta mass and kinetic energy, compared to the pseudo-bolometric light curve. While an increase of the physical parameters is expected, the difference in physical parameters is not expected to great enough to alter any of the conclusions derived from the analysis of pseudo-bolometric light curve.

The evolution of the pseudo-bolometric light curve of SN 2020acat, along with the light curves of of SN 1993J, SN 2008ax, SN 2011dh, SN 2011fu, SN 2013df, and SN 2016gkg are displayed in Fig. 6, with the peak time evolution of each pseudo-bolometric light curve shown in the upper right-hand plot. These SNe were used as comparison objects for SN 2020acat due to their comprehensive photometric coverage, which extends from the early time to well in to the nebular time phase. This allows for their pseudo-bolometric light curves to be compared with that of SN 2020acat during both the pre-maximum and post maximum phases, as well as at late time when ^{56}Co decay dominates the light curve. All SNe shown in Fig. 6 have also been thoroughly modelled and have well determined properties such as distance modulus, extinction and explosion date. This allows for a comparison and permits the placement of SN 2020acat within the property distribution space of SNe IIb. Also shown in Fig. 6 is the decay slope of ^{56}Co, the source of power expected to dominate the late-time evolution of SNe. As expected, the decay of SNe IIb display a small spread at late time with all light curves significantly diverging from the slope of ^{56}Co decay (Wheeler, Johnson & Clocchiatti 2015), as predicted when there is an the absence of the full trapping of the gamma-rays released by the decay of ^{56}Co.

The pseudo-bolometric light curve of SN 2020acat peaks at a luminosity of $L_{\rm peak} = 3.09^{+1.28}_{-0.9} \times 10^{42}$ erg s^{-1}, $Log(L_{\rm peak}) = 42.49 \pm 0.15$ [erg s^{-1}], with a rise time of ∼14.6 ± 0.3 d. The rise time of SN 2020acat is considerably faster compared to the other SNe IIb, which tend to have a rise time of ∼20 d or longer, and was expected from the rapid rise seen in the UV and optical bands. The pseudo-bolometric light curve of SN 2020acat lacks any shock-cooling tail seen in several of the other SNe IIb. While it may be possible that the shock-cooling phase of SN 2020acat was fully missed, this is unlikely

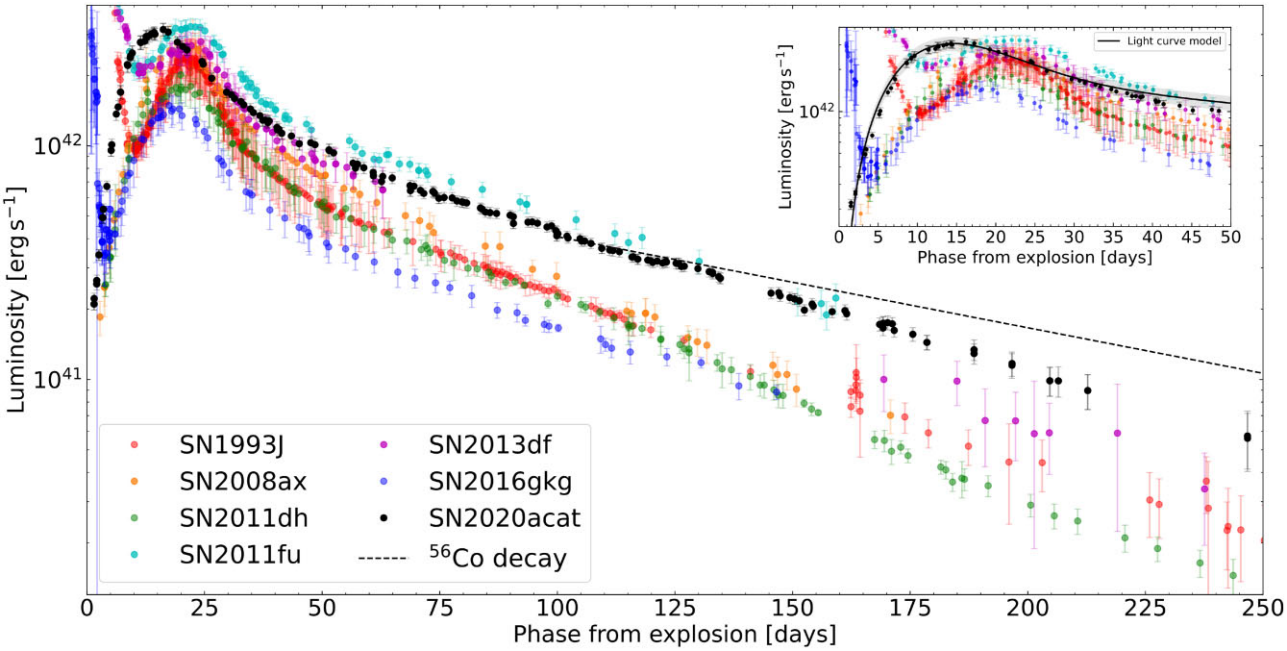

Figure 6. The pseudo-bolometric light curve of SN 2020acat, along with several other well-observed SNe IIb over the first 250 d. The SNe shown in the plot are SN 1993J (red), SN 2008ax (orange), SN 2011dh (green), SN 2011fu (cyan), SN 2013df (magenta), SN 2016gkg (blue), and SN 2020acat (black). All SNe have been corrected for reddening as well as time dilation. The black dashed line displays the cobalt decay line that should dominate at late times for light curves powered solely by the decay of ^{56}Ni. The subplot (upper right) displays the initial 50 d of each pseudo-bolometric light curves. For SN 2020acat, the Arnett-like fit is also displayed by the solid black line, along with associated errors for the model shown by the grey shaded region. The physical parameters of each SN IIb obtained from the Arnett-like fit are given in Table 4.

to have happened. The extended duration of the shock-cooling phase combined with the luminous nature of the shock-cooling tail, which tends to outshine the peak of the ^{56}Ni powered peak of the light curve, makes it a very obvious feature of the light curves of SNe IIb when it is present. Thus, the lack of evidence for the light curve of SN 2020acat showing any dimming from an initial bright peak and the tight restriction on SN 2020acat's explosion date, make it likely that the shock-cooling phase of SN 2020acat was not prominent, a feature that is associated with SN from compact progenitors as was seen with SN 2008ax.

SN 2020acat displays a higher peak luminosity than the majority of SNe IIb shown in Fig. 6. Among the SNe of our sample, only SN 2011fu is of similar brightness to SN 2020acat, with a peak luminosity of $\mathrm{Log}(L_{\mathrm{peak}}) = 42.49 \pm 0.17[\mathrm{erg\,s^{-1}}]$, while SN 2008ax has a similar luminosity to SN 2020acat, peaking at a luminosity of $\mathrm{Log}(L_{\mathrm{peak}}) = 42.38 \pm 0.57[\mathrm{erg\,s^{-1}}]$. Compared to the mean peak luminosity for SNe IIb given by Prentice et al. (2016), $\mathrm{Log}(L_{\mathrm{peak}}) = 42.36 \pm^{0.26}_{0.11}$ [erg s^{-1}], SN 2020acat is $\sim$0.12[erg s^{-1}] brighter, suggesting that a larger than average amount of ^{56}Ni was synthesized during the explosion. The analysis done in Prentice et al. (2016) makes use of the same cosmology as used in Section 2 allowing for a comparison with SN 2020acat to be made.

However while a valid comparison to SN 2020acat can be made, it should be noted that there is an additional uncertainty in the luminosity of SN 2020acat and several comparison objects. This error arises from uncertainties in the distance modulus for events that lacked redshift independent distances and sit outside the Hubble flow, as mentioned in Section 2. However, the uncertainty is not expected significantly alter the peak luminosities obtained for the SNe IIb shown here, as the bolometric corrections are the main contributor to the error for the pseudo-bolometric light curves.

An Arnett-like model (Arnett 1982) was fit to the pseudo-bolometric light curves of SN 2020acat and the other SE-SNe to determine the mass of ^{56}Ni synthesized, as well as the mass of material ejected by the explosion (M_{ej}) and the SNe kinetic energy (E_{k}). For the fitting of the Arnett-like model, an opacity of $\kappa = 0.06\,\mathrm{cm^2\,g^{-1}}$ and a dimensionless form factor derived by Arnett (1982) of $\beta = 13.8$, were used for all SNe. An opacity of $0.06\,\mathrm{cm^2\,g^{-1}}$ was used here as it has been established that a small optical opacity is needed for the modelling of the bolometric light curves for hydrogen rich SNe, and has been used in studies of SNe IIb (Lyman et al. 2016). The degeneracy between the ejecta mass and the kinetic energy was broken for each SN by using the photospheric velocity, v_{ph}. For SN 2020acat, the photospheric velocity had a value of $\sim$10 000 $\pm$ 1000 km s^{-1}. The method used to obtain the photospheric velocity discussed in Section 5.2. Additionally, the model used for SN 2020acat and the other SNe IIb was slightly modified to determine the estimated explosion date by fitting to the pre-peak photometric data. This was modified for those SNe that displayed a shock-cooling phase and produced values all within the error range given for the explosion date within the literature.

The Arnett-like model, shown in the upper right-hand plot of Fig. 6, is well fitted to the peak of the pseudo-bolometric light curve and the majority of the rise time. Although, it seems to underestimate the luminosity of the initial points, within less than 5 d from explosion, and starts to diverge away from the constructed pseudo-bolometric light curve at around 35–45 d after estimated explosion. The divergence at later times, $\geq$35 d, is expected as the light curve transitions away from being dominated by solely the decay of ^{56}Ni. Interestingly, the underestimation of the bolometric light curve at the earliest phase implies that the mass of ^{56}Ni is more mixed into the outer ejecta than what the model assumes. The main errors

Table 4. Light-curve details and physical parameters derived from fitting the pseudo-bolometric light curves for SN 2020acat and the other SNe IIb with the Arnett-like fit.

SN	Log(L_{peak}) (erg s^{-1})	t_{peak} (d)	v_{ph} ($\times 10^3$ km s^{-1})	This work M_{Ni} ($M_\odot$)	This work M_{ej} ($M_\odot$)	This work E_k ($\times 10^{51}$ erg)	Literature M_{Ni} ($M_\odot$)	Literature M_{ej} ($M_\odot$)	Literature E_k ($\times 10^{51}$ erg)
2020acat	42.49 ± 0.15	14.62 ± 0.27	10.0 ± 0.5	0.13 ± 0.03	2.3 ± 0.4	1.2 ± 0.3	–	–	–
1993J	42.37 ± 0.17	19.95 ± 0.32	8.0 ± 1.0	0.10 ± 0.03	1.9 ± 0.4	0.7 ± 0.2	0.10 ± 0.04	2.7 ± 0.8	1.3 ± 0.3
2008ax	42.38 ± 0.08	17.20 ± 0.27	7.5 ± 0.5	0.13 ± 0.04	2.5 ± 1.0	0.8 ± 0.3	0.10 ± 0.02	2.7 ± 0.5	1.2 ± 0.5
2011dh	42.15 ± 0.11	20.21 ± 0.54	6.5 ± 1.0	0.05 ± 0.01	2.2 ± 0.4	0.6 ± 0.1	0.07 ± 0.01	2.1 ± 0.5	0.8 ± 0.2
2011fu	42.49 ± 0.14	21.15 ± 0.73	8.0 ± 1.0	0.17 ± 0.03	3.4 ± 0.7	1.3 ± 0.3	0.15	3.5	1.3
2013df	42.38 ± 0.07	17.84 ± 0.30	8.0 ± 1.0	0.11 ± 0.02	1.5 ± 0.3	0.6 ± 0.1	0.11 ± 0.02	0.11 ± 0.30	0.8 ± 0.4
2016gkg	42.13 ± 0.02	18.47 ± 0.13	8.0 ± 1.0	0.06 ± 0.01	1.6 ± 0.3	0.6 ± 0.1	–	–	–

Notes. Shown on the left are the literature values for the M_{Ni}, M_{ej}, and E_k of the different SNe IIb, these values were derived using the Arnett-like model and an optical opacity $\kappa = 0.06\,cm^2\,g^{-1}$.

associated with the model arise from the error in the photospheric velocity, the error associated with the pseudo-bolometric light curve and the error within the estimated explosion data. From the fitting to the pseudo-bolometric light curve, the values for the physical parameters of SN 2020acat and the comparison SNe IIb, along with the peak luminosity and rise time for each event were determined. These values along with the photospheric velocity used to break the degeneracy between M_{ej} and E_k, are given in Table 4. From the modelling of the SN 2020acat light curve, a ^{56}Ni mass of $M_{Ni} = 0.13 \pm 0.03$ M$_\odot$ was obtained, along with a ejecta mass of $M_{ej} = 2.3 \pm 0.4$ M$_\odot$ and a kinetic energy of $E_k = 1.2 \pm 0.3 \times 10^{51}$ erg. It should be noted that in recent years, there has been a lot of discussion in the validity of using an Arnett-like approach to obtain the value of the ^{56}Ni mass synthesized by CC-SNe. Khatami & Kasen (2019) discussed the effect of neglecting the time-dependent diffusion on the ^{56}Ni mass that Arnett-like models assume. Alternative models for CC-SNe have shown that the value of ^{56}Ni mass derived from the Arnett-like model is higher by ∼30–40 per cent than the results from recent modelling (see Dessart et al. 2016; Woosley, Sukhbold & Kasen 2021). As such if the ^{56}Ni mass derived above for SN 2020acat is overestimated by ∼30–40 per cent then the final ^{56}Ni mass for SN 2020acat would be $M_{Ni} = (0.08–0.09) \pm 0.03$ M$_\odot$. However due to the prolific use of the Arnett-like model in the literature, when comparing the physical parameters of SN 2020acat with those of other SNe IIb, the uncorrected value of M_{Ni} will be used to give a more valid comparison.

The physical parameters obtained for SN 2020acat suggests that it was a high-energy event, producing a large amount of both ^{56}Ni and ejecta. However, to get a comprehensive look at the physical parameters of SN 2020acat a comparison with a large study of SNe IIb is needed. From Prentice et al. (2019), a mean value of M_{Ni} and M_{ej} of SNe IIb were determined to be 0.07 ± 0.03 and 2.7 ± 1.0 M$_\odot$, respectively. These physical parameters show that SN 2020acat produced a roughly average value for the ejecta mass while having a significantly higher value for the nickel mass, which would account for the brighter pseudo-bolometric light curve shown in Fig. 6. However, when compared to the analysis of SE-SNe done by Lyman et al. (2016), with values of $M_{Ni} = 0.11 \pm 0.04$ M$_\odot$, $M_{ej} = 2.2 \pm 0.8$ M$_\odot$ and a kinetic energy of $1.0 \pm 0.6 \times 10^{51}$ erg, SN 2020acat synthesized slightly more nickel than the average SNe IIb, an average amount of ejecta mass and a slightly higher kinetic energy. From both study comparisons it can be seen that SN 2020acat is an energetic event that produces a roughly average amount of ejecta for an SN IIb.

The high energy derived for SN 2020acat, along with the value of M_{ej}, supports the idea that the progenitor of SN 2020acat was an intermediate mass star with an M_{ZAMS} between 15 and 20 M$_\odot$. The progenitor mass range of SN 2020acat was determined using the derived physical parameters, along with an assumed remnant mass of 1.5–2.0 M$_\odot$, and the progenitor models described in Sukhbold et al. (2016). The value of the M_{ZAMS} predicted for SN 2020acat, while on the higher end of progenitor masses, is not out of the range of possibility for an SE-SNe. Deng et al. (2003) reported a similar progenitor M_{ZAMS} ∼20–25 M$_\odot$, for SN 2002ap, an SN Ic that produced a similar amount of ejecta mass as SN 2020acat. A high-mass progenitor, M_{ZAMS} ∼18 M$_\odot$, was also suggested by Folatelli et al. (2015) for SN 2008ax. It was also shown by Lyman et al. (2016) that the observed distribution of ejecta masses for SE-SNe can be explained by progenitors with masses that range between 8 and 20 M$_\odot$. As such, an intermediate- to high-mass progenitor for SN 2020acat is not impossible, although it would require detailed hydrodynamic modelling to determine its validity, which is beyond the scope of this work.

5 SPECTROSCOPIC ANALYSIS

Fig. 3 shows the spectral evolution of SN 2020acat until the start of the nebular phase. The initial spectrum of SN 2020acat was obtained on December 10, 2020 (MJD = 59193.31), approximately 1 d after the estimated explosion date. Initially, the spectra of SN 2020acat displayed a blue continuum due to the high temperature of the material, before rapidly cooling. At around +20 d from explosion, the blue continuum had faded and the spectral-line features become more dominant. The Hα feature, along with Hβ and to a lesser degree Hγ, dominate the spectra for the first ∼100 d. Helium features are also clearly present, although they are not as strong as the hydrogen ones, as well as some ionized iron features. After ∼100 d, the hydrogen features have almost fully faded from the spectra, leaving both oxygen and calcium to dominate the spectra of SN 2020acat, as the photosphere recedes deeper into the ejecta and the spectra transitions into the nebular phase.

5.1 Early phase

5.1.1 Pre-maximum light

During the pre-maximum light phase, ∼0–20 d after explosion, the Hα feature displays a strong broad P-Cygni profile. While hydrogen features are clearly visible throughout the photospheric phase, the He I λλ5876, 6678, 7065 lines do not produce strong features until post-max light (∼25 d after explosion), with the 5876 Å being the strongest of the He I features, and the only one clearly visible in the

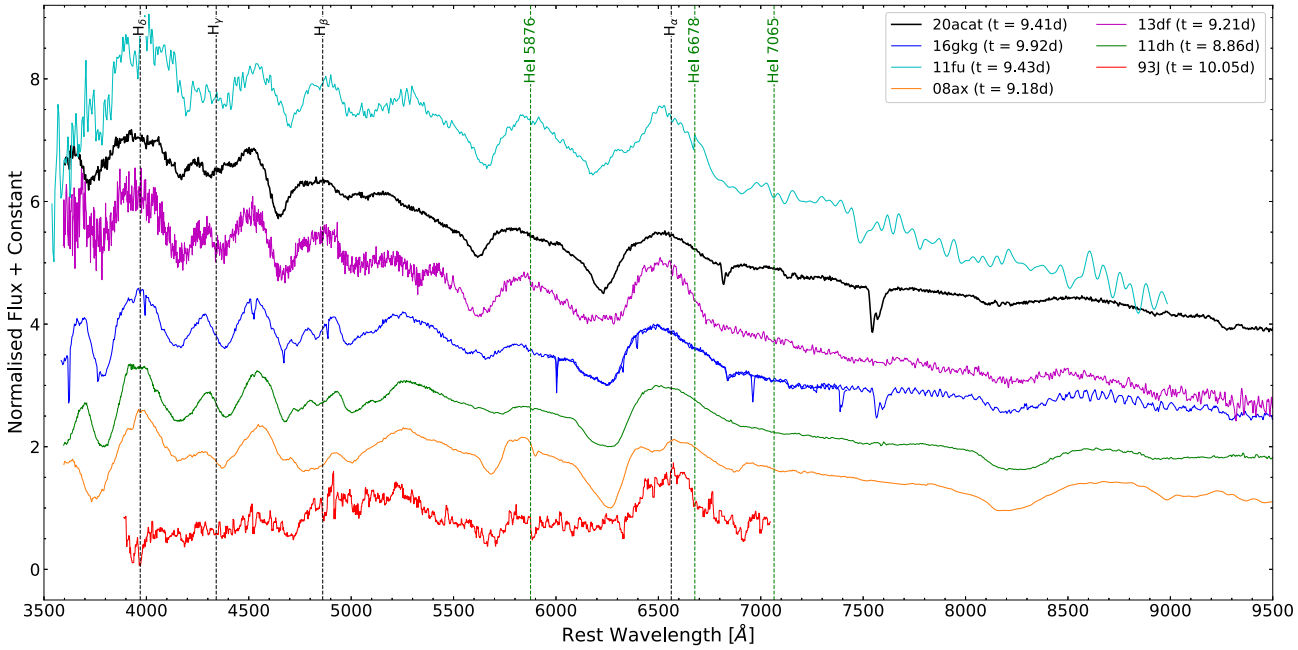

Figure 7. Spectroscopic comparison of SN IIb at around 9 d from explosion. All spectra have been corrected for redshift and extinction. The emerging hydrogen and helium features are marked at their rest wavelength.

pre-max spectra. The 6678 Å feature is especially weak and seems to disappear when the H α feature is no longer visible.

In the blue region (< 6000 Å) of the optical spectra, where the Fe II line features usually dominate, there is a strong absorption feature at ∼4900 Å that is of similar depth to the H β feature at around ∼20 d after the explosion. This feature is generally identified as Fe II λ5018. However, it is generally observed alongside other Fe II lines, all of which display a similar strength. This is not what is observed in the spectra of SN 2020acat, where the Fe II 5018 feature broadly dominates over the other Fe II features. Also, the 4900 Å component is not broad enough to be a result of both the Fe II λλ4924, 5018 blending together, and there is a distinct weak absorption component between the H β line and the 4900 Å feature that has been associated with the Fe II λ4924 line. The existence of a distinct Fe II λ4924 feature, along with the fact that both the 4924 Å and 5169 Å components are not of similar strength relative to the 5018 Å line place strong doubt on the origins of the 4900 Å feature as the result of solely a Fe II line. The question remains on what is the element that causes the 4900 Å feature, within the spectra of SN 2020acat. This was tested by fitting the spectra of SN 2020acat with a continuum fit and adding an absorption component of different elements that possess a strong emission line just redward of the 4900 Å. Once the likely elements were identified, a line velocity was determined from the absorption minimum. The velocity was used to fit the features of the elements other optical lines found in different regions of the spectrum. If the additional features matched up with several other absorption features within the spectrum the element was considered a likely source of contribution to the 4900 Å feature. The process was repeated three times to determine if the elements presence existed within the spectra or if the initial presence was due to the noise within the spectrum. From this testing, the best elements that would have been able to create the 4900 Å feature are either helium, nitrogen or a combination of both, enhancing the already existing Fe II λ5018 line. The helium line that would result in the 4900 Å feature is the He I λ5016 line, which is significantly weaker than the He I λ5876, with a weighted transition probability $g_k A_{ki}$ of 4.0116×10^7 and 4.9496×10^8, respectively (Drake 2006), thus making it unlikely that the He I λ5016 line is the only line responsible for the 4900 Å feature. Along with helium, nitrogen also possesses multiple optical lines whose presence were identified from fitting the spectra of SN 2020acat during the post-maximum brightness and the spectra observed between the photospheric phase and the nebular phase. These lines being the N II λλλ5005, 5680, and 5942 lines, which have equivalent transition probability to the He I λ5876 line with a value of $g_k A_{ki}$ of 3.63×10^8 (Luo & Pradhan 1989), 3.47×10^8 (Tachiev & Fischer 2001), and 5.47×10^7 (Tachiev & Fischer 2001), respectively. There also exists a weak N II line at 6482 Å, however this line overlaps with the H α feature thus making the determination of its presence at early times, where the hydrogen Balmer features dominate, quite difficult. While the presence of additional nitrogen may enhance the broad nature of the 4900 Å feature, through the blending of several lines within the iron region of the SN 2020acat spectra, it should be noted that nitrogen does not have a strong emission. As such, the presence of nitrogen alone is not enough to strongly alter the spectrum of SN 2020acat, unless unrealistic amounts of nitrogen were to be introduced. Therefore, while it is possible that nitrogen enhances the existing feature, the main cause of the 4900 Å feature is still thought to be a result of helium and iron.

The pre-maximum spectrum of SN 2020acat, taken on December 18, 2020, at around 9 d after explosion, was compared to the spectra of five SN IIb, each taken at a similar epoch, in Fig. 7. All spectra have been corrected for reddening, given in their rest wavelength, and normalized to the peak of the H α feature. Unfortunately, SN 1993J lacked full wavelength coverage at this epoch, covering a range of ∼4000–7000 Å. However, in this phase, as the major feature at wavelengths redder than 7000 Å is the Ca II feature the missing section of SN 1993J is not expected to be of great concern. Relative to the other SNe IIb, SN 2020acat displays broader features for all lines seen at this epoch. SN 2020acat also displays strong hydrogen features compared to the other SNe. Unlike SN 2008ax, SN 2011dh,

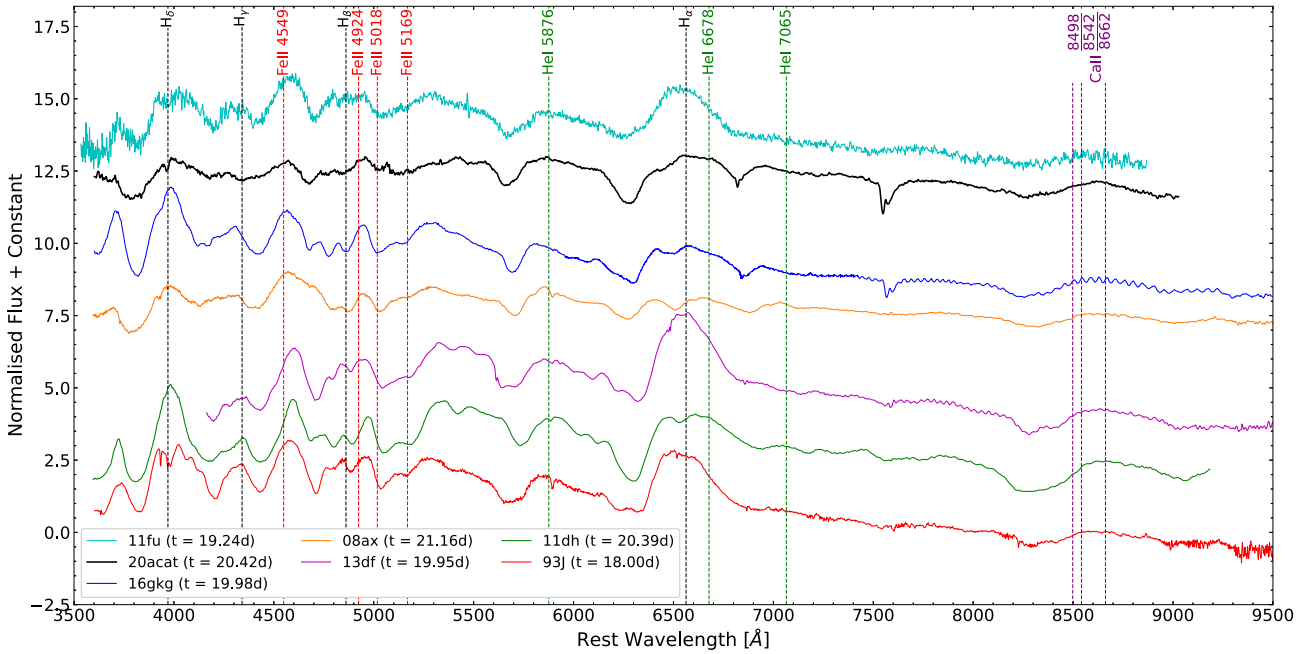

Figure 8. Spectral comparison of SN 2020acat with several well-observed SNe IIb roughly 20 d after explosion. Phase from explosion date for individual SNe is given in the legend. All spectra are shown in the rest frame and were normalized to the peak of the H α feature. SNe are ranked in terms of the He I λ5876 line velocity and given in the rest frame. Key photospheric phase lines are marked by the dashed lines and are given at their rest wavelength.

and SN 2016gkg, SN 2020acat lacks strong iron features at around ~4800 Å, instead showing a smooth emission from H β. The depth of the Ca II H&K feature within the spectrum of SN 2020acat is not as deep relative to some of the other SNe, being similar to both SN 2013df and SN 2016gkg.

5.1.2 Post-maximum light

The spectrum of SN 2020acat at ~20 d post-explosion was also compared to the other SNe IIb at a similar epoch, in Fig. 8, which have been ranked by the He I λ5876 maximum velocity. As expected, SN 2020acat displays a very blueshifted helium feature with only the helium feature of SN 2011fu being bluer in wavelength. In all SNe spectra, the He I λ5876 feature is strong and displays very similar shape in all except SN 1993J and SN 2013df. The H α feature, while present in all spectra at this epoch, varies significantly in both strength and broadness among the different SNe IIb displayed in Fig. 8. In SN 2020acat, the H α emission is quite broad, such that the He I λ6678 feature is visible within the emission component P-Cygni H α profile, just blue of the peak. In all spectra, the H α P-Cygni absorption feature is deeper than He I λ5876, although in the spectrum of SN 2008ax, both features have a very similar depth. Unlike both SN 1993J and SN 2013df, SN 2020acat does not display a broad flat minimum in either the H α and He I λ5876 features, showing that within SN 2020acat the hydrogen and helium existed within distinct shells and lack multiple high-density regions as suggested for SN 1993J and SN 2013df (Sahu et al. 2013). All spectra also display clear NIR Ca II features. It should be noted that the line velocity of all major features, in the ~20-d spectrum of SN 2020acat, are faster than those of other SNe at the same epoch, this can be clearly seen in Fig. 9. The high velocity of all major features suggests that SN 2020acat was a very energetic event, likely originating from a high-mass progenitor star.

5.2 Line velocity evolution

The expansion velocity of the ejected material in SN 2020acat was measured from of the P-Cygni profiles for the H α, H β, He I λ5876, and Fe II λ5018 lines within the spectra prior to day 100. This was determined by fitting the absorption minimum of the line profiles with a Gaussian function. The main error associated with the line velocity originates from the noise of the individual spectrum, along with a small error associated with fitting of the line features and the redshift correction. However, due to the high S/N of the spectra, the error at most epochs is not large for the H α, H β, and He I λ5876 lines.

Unlike the other lines, the Fe II λ5018 line has an additional error associated with the origin of the 4900 Å feature. As mentioned in Section 5, identification of the Fe II λ5018 line is made difficult by the presence of helium and potentially nitrogen lines, and due to line blending, as well as the resolution of the spectra, it is not possible to determine the velocity minimum of each line individually. Despite that, we expect the velocity profile of the feature to be dominated by the Fe II λ5018 line and have taken the minimum of the 4900 Å as the maximum velocity of the Fe II λ5018 with an additional error of ~20 per cent from the blending of the helium and possibly nitrogen lines. Due to the trouble with identifying the Fe II λ5018 line, the line velocities other Fe II lines were used to check the obtained Fe II λ5018 line velocity evolution with all lines showing an agreement with the velocity range derived for the Fe II λ5018 line.

Along with the line velocity of the Fe II λ5018 line, measuring the expansion velocity of the Fe II λ5169 line is critical in determining the velocity of the photosphere as it moves through the expanding ejecta. Both Hamuy et al. (2001) and Takáts & Vinkó (2012) have shown that the evolution of the Fe II lines closely follow the evolution of the photosphere, especially compared to other lines seen during the photospheric phase such as the Balmer lines (Dessart & Hillier 2005). Due to the nature of the Fe II region discussed in Section 5.1.1

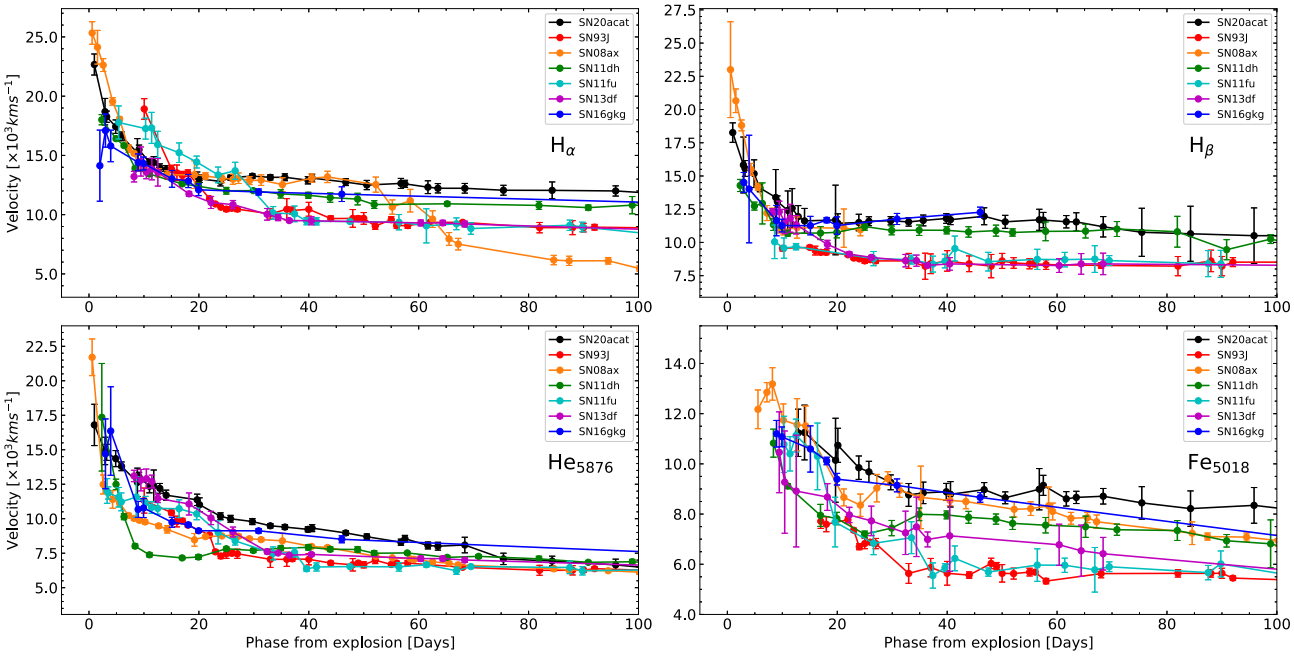

Figure 9. Line velocity evolution of the H α, H β, He I λ5876, and Fe II λ5018 lines for SN 2020acat, which are compared to those of other SNe IIb, over the first 100 d from explosion. It's clearly seen that SN 2020acat displays one of the highest line velocities of the SNe shown here.

and the noise within the spectra of SN 2020acat, determining the velocity of the Fe II λ5169 line at maximum light resulted in a large velocity uncertainty. Despite that a photospheric velocity, based on the Fe II λ5169 line, of $v_{\rm ph} \sim 10\,000 \pm 1000$ km s^{-1} was determined from the peak time spectrum, taken $\sim$15.5 d after explosion.

The velocity evolution of these lines was compared to the velocity evolution obtained from SN 1993J, SN 2008ax, SN 2011dh, SN 2011fu, SN 2013df, and SN 2016gkg in Fig. 9. Overall, the line velocities of elements identified in SN 2020acat are consistently higher when compared to other SE-SNe. The H α velocity initially is rivalled by only SN 2008ax at $\sim$22 700 km s^{-1}, being $\sim$1000 km s^{-1} higher than the other SNe. The H α and H β velocities rapidly decline over the first $\sim$20 d, before plateauing at around $\sim$13 000 and $\sim$12000 km s^{-1}, respectively. Both the H α and H β of SN 2020acat display a slight increase in their velocity of $\sim$500 km s^{-1} at around $\sim$30 d. This increase likely results from the fitting of the spectra as there is no physical reason seen within either the spectra or light curve that would account for this increase in velocity. The He I λ5876 feature of SN 2020acat starts at $\sim$16 800 km s^{-1} and steadily declines for $\sim$70 d, remaining higher than the other SE-SNe, until SN 2020acat starts to transition into the nebular phase. The Fe II λ5018 line velocity of SN 2020acat remains faster than other SNe throughout the spectroscopic evolution.

5.3 Transition into the nebular phase

Between $\sim$50 and 120 d after the explosion, the spectrum of SN 2020acat undergoes a drastic change as the Balmer lines become narrower and more shallow, and the photosphere recedes deeper into the expanding ejecta. Along with the fading of the hydrogen features, the line velocity of most elements drops at a much slower rate than during the photospheric phase, falling by $\sim$2000 km s^{-1} during this period, although the H α and H β lines drop at a slower pace only decreasing by $\sim$1000 km s^{-1}. The He I lines increase in strength relative to the H α line, and become the dominant feature as the spectrum transitions into that of an SN Ib. While this is happening, the NIR Ca II $\lambda\lambda$8498, 8542, 8662 feature also becomes stronger, along with the weak absorption component of the Ca II H&K lines. Towards the end of this phase, the [Ca II] lines $\lambda\lambda$7291, 7324, along with the allowed O I λ7773 feature, start to appear showing the spectrum is transitioning into the nebular phase.

The spectrum of SN 2020acat at $\sim$60 d is compared with spectra of the other SNe IIb at a similar epoch, although the spectrum of SN 2016gkg is $\sim$15 d earlier than the rest due to the limited late time observations, in Fig. 10. Despite the late time, the absorption component of the H α feature in the SN 2020acat is much deeper than in the other SNe IIb. This deep hydrogen feature suggests that a large amount of hydrogen is still present at the depth of the photosphere at around $\sim$60 d after the explosion. The presence of strong hydrogen features at this epoch may result from the progenitor having hydrogen mixed throughout the outer envelope and into parts of the inner envelope prior to collapse. The H α feature is also still significantly broader than those seen for other SNe IIb.

Although the H α feature remains broad in SN 2020acat, the He I velocities have dropped to within the velocity distribution given by the other SNe IIb. Overall, the spectrum of SN 2020acat at this epoch is similar to that of SN 2016gkg, which still displays a relatively strong H α feature. Although, it should be noted that the spectrum of SN 2016gkg is $\sim$15 d earlier than that of SN 2020acat, which can drastically change the strength of the H α feature and thus would affects the similarity between these two SNe. The H α and He I λ5876 features within all spectra are of similar widths and all SNe display strong Ca II features in the NIR region, with both SN 1993J and SN 2008ax displaying a double-peaked profile. The region within the spectra of SN 2020acat between 4800 and 4900 Å displays both a noticeable H β and a broad feature within the Fe II portion of the region. This strong feature at this epoch is unlikely to result of solely Fe II lines and as discussed in Section 5.1.1 is expected to be enhanced by the presence of helium and possible nitrogen. If the $\sim$4900 Å feature is indicative to the presence of

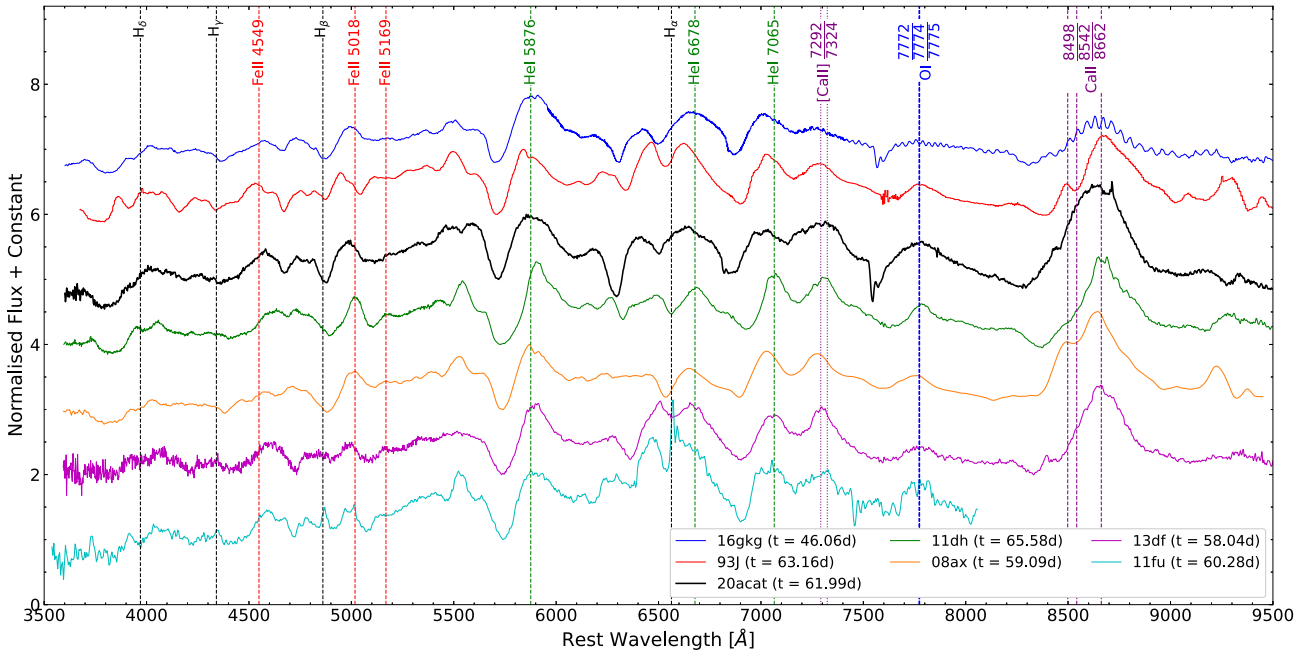

Figure 10. Spectral comparison of SN 2020acat with several well-observed SNe IIb roughly 60 d after their reported explosion date. All spectra are shown in he rest frame and are ranked in terms of He I λ5876 line velocity. Key transition phase element lines are marked at their rest wavelength, with allowed transitions shown as the dashed lines and forbidden lines shown as dotted lines.

nitrogen in the spectra of SN 2020acat, it is expected that there should be other N II features detected, including the N II λλ5680, 6611 lines. These lines can be associated with weak features seen in the ∼60-d spectrum of SN 2020acat in Fig. 10, at ∼5500 and 6450 Å, respectively. The feature potentially produced by the N II λ5680 line is located blue of the [O I] λ5577 feature, which produces a strong emission feature in all spectra except for SN 2013df and SN 2020acat. The potential N II 6611 Å feature could be associated with a weak absorption feature between the H α peak and the He I λ6678 absorption minima. The 6611 Å feature is significantly weaker than the 5680 Å and 4900 Å features, likely due to a combination of the hydrogen and helium dominating the spectrum in this region. All of these absorption features are associated with nitrogen corresponding to a line velocity of ∼8000 ± 500 km s^{-1}, suggesting that, if present, they all result from the same nitrogen-containing shell. Jerkstrand et al. (2015) discuss models that display strong N II within the late time (>100 d). In order to determine the existence of potential N II lines, more detailed modelling of the spectrum at these epochs are required, which is beyond the scope of this work.

5.4 Nebular phase

At around ∼120 d after the explosion of SN 2020acat, the spectrum transitions into the nebular phase. During this phase, the H α feature completely disappears and the He I features decrease in strength. While this is happening, both the [O I] λλ6300, 6363 and the [Ca II] λλ7291, 7323 doublets become stronger and dominate the spectrum. The spectrum of SN 2020acat at ∼170 d was compared to several SNe IIb at the same epoch, see Fig. 11. Once again, the spectrum of SN 2016gkg differs significantly in phase compared to the other SNe. All the spectra of the SNe shown in Fig. 11 are dominated by either the [O I] λλ6300, 6363 or the [Ca II] λλ7291, 7324 feature at this epoch. Mg I] λ4571, O I λλ7772, 7774 and the NIR Ca II are also all identified within the spectrum of SNe IIb at this epoch. During this phase, the spectrum of SN 2020acat appears most similar to that of SN 1993J, both dominated by the [O I] feature over the [Ca II] feature. Both of these SNe lack a spectral feature at around 5700 Å, which is present in the SNe that are dominated by [Ca II]. While they are similar SN 2020acat does not display a double peak in the Ca II NIR feature seen in SN 1993J, along with several other SNe IIb, instead possessing a single Ca II NIR peak seen also in SN 2016gkg. Another difference between SN 2020acat and SN 1993J is the lack of a small feature around 6400 Å, associated with H α. This suggests that hydrogen in SN 2020acat, while mixed deep into the outer layers of the progenitor star as indicated by the strong H α visible at earlier epochs, is unlikely to penetrate deep into the inner layers or exist in a thick circumstellar medium.

Both the [O I] and [Ca II] features observed within nebular time spectra can be used to probe the asymmetrical nature of the ejecta, as done with SN 2003bg by Mazzali et al. (2005). The evolution of the shape of both the [O I] and [Ca II] peaks in the spectra of SN 2020acat are shown in Fig. 12. The spectrum on day 117.04 still displays the remnant of an H α feature, seen by the flat-topped profile that would not be present if only [O I] was emitting in that region. Once the H α feature has fully faded from the spectrum, at ∼130 d, the [O I] feature displays a strong symmetric shape. When compared with the [O I] features of other SE-SNe, the [O I] of SN 2020acat does not display a strong double-peaked feature, and appears more similar to both SN 2011fu and SN 2013df. Instead, the nebular spectra of SN 2020acat display a small bump on the red side of the peak, which is due to the [O I]λ6363 line. The centroid of the [O I] peak is aligned with the 6300 Å, while the centroid of the [Ca II] peak is slightly shifted by ∼1000 km s^{-1}, which seems to move towards zero velocity as the spectra evolve. The [Ca II] feature is broader than those of other SNe IIb by several thousand km s^{-1}, likely a result of the high explosion energy causing a large dispersion in the calcium velocity distribution.

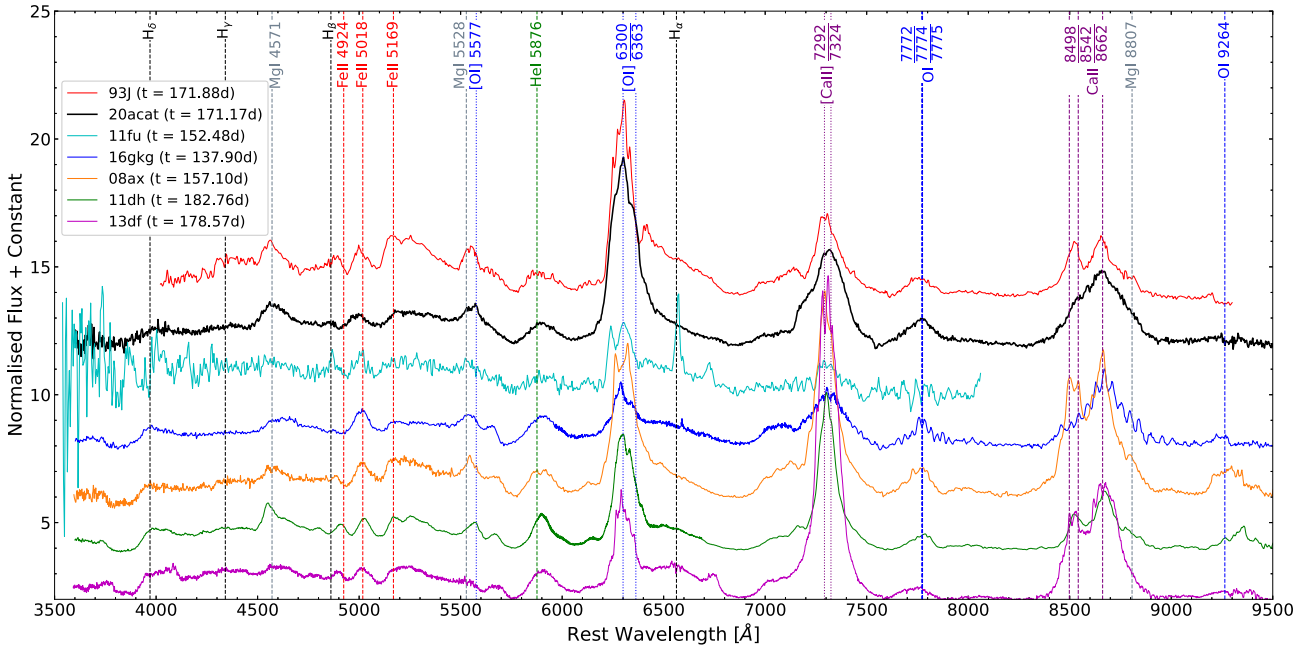

Figure 11. Spectral comparison of SN 2020acat with several SNe IIb around day ∼170. Phase from the explosion date is given in the legend and all spectra are shown in the rest frame. SNe are ordered with respect to the flux ratio of the [O I] and [Ca II] nebular features. Key nebular phase line features are marked at their rest wavelengths, with allowed transitioned shown as the dashed lines and forbidden lines shown as dotted lines.

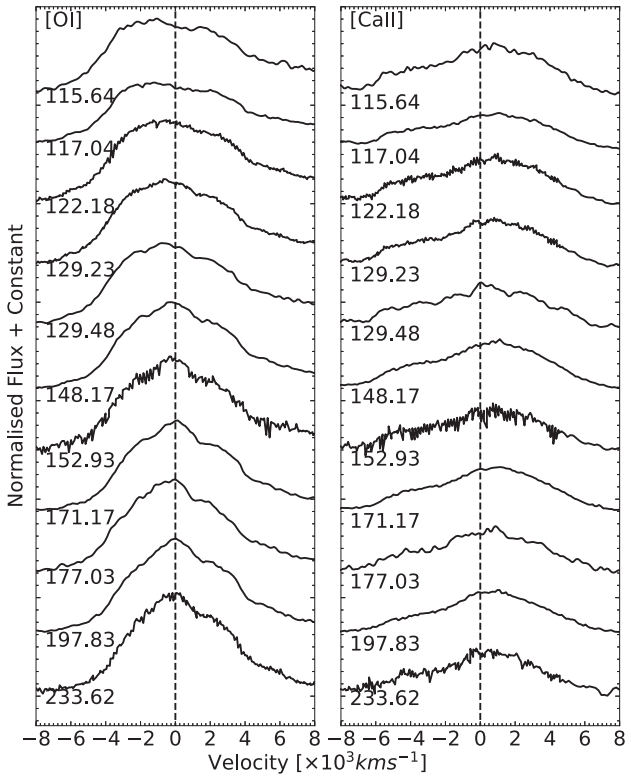

Figure 12. Line profile of [O I] λλ6300, 6363 (left) and [Ca II] λλ7292, 7324 (right) within the late-time spectra of SN 2020acat. The dashed lines are the emission velocities corresponding to 6300 and 7291 Å lines. The epoch from estimated explosion date for each spectrum is given in the rest frame.

5.5 Oxygen mass and [Ca II]/[O I] ratio

Fransson & Chevalier (1989) suggested that the ratio between the flux of the [Ca II] λλ7291, 7324 and the [O I] λλ6300, 6363 lines provides a good way of estimating whether the progenitor had a large or small main-sequence mass. This is due to the assumption that the flux of the oxygen emission region is directly related to the mass of oxygen formed throughout the evolution of the progenitor star, while the flux of the calcium emitting region is dependent solely on the mass of calcium synthesized during the explosion, and thus not effected by the mass of the progenitor during its life cycle. Therefore, a large ratio, [Ca II]/ [O I]$\gtrsim\sim 1$, is expected to be the result of the progenitor having a small main-sequence mass. It was shown by Elmhamdi et al. (2004) that the [Ca II]/[O I] ratio within the spectrum at late enough times (>150 d) is expected to stay stable over very long periods. For SN 2020acat, at ∼170 d, the [Ca II]/[O I] ratio was found to be ∼0.5, similar to that seen for SN 1993J and SN 2011fu at similar epochs, which suggests that the progenitor of SN 2020acat had a large $M_{\rm ZAMS}$. However, it should be noted that this method is not a robust tool for obtaining $M_{\rm ZAMS}$. The ratio between the [Ca II] λλ7292, 7324 and [O I] λλ6300, 6363 varies strongly among the different SNe IIb displayed in Fig. 11, with SN 2008ax, SN 2011dh and SN 2013df all displaying a stronger forbidden calcium feature relative to the oxygen peak. SN 1993J, SN 2011fu, SN 2016gkg, and SN 2020acat, on the other hand, all show a stronger oxygen feature that dominates over the calcium, although with SN 2016gkg, the peaks of the oxygen and calcium features are very similar at ∼140 d. Caution, however, should be taken with the spectrum of SN 2016gkg that was obtained ∼30 d earlier than the other SNe and thus, by day 170, may have a drastically different ratio, especially given the proximity to unity that the [Ca II]/[O I] ratio had at ∼140 d.

From the nebular phase spectra of SN 2020acat, an estimation of the oxygen mass can be made, which can provide insight into the expected progenitor mass. The relationship between the observed [O I] emission peak and the mass of oxygen was described by Uomoto

Table 5. Mass of oxygen obtained from the late-time spectra of SN 2020acat using equation (4).

Phase (d)	Flux ($\times 10^{-14}$ erg s^{-1} cm^{-2})	$M_{\rm O}$ ($M_\odot$)
171.17	8.407	3.13 (0.14)
177.02	7.406	2.76 (0.10)
197.83	7.691	2.87 (0.12)
233.62	2.590	0.97 (0.04)

Notes. The flux from the spectrum taken 171.17 d from explosion is taken as an upper limit to the mass of oxygen. The error associated with each epoch is given in the parenthesis.

(1986), which is expected to hold within a high-density limit ($N_{\rm e} \geq 10^6 {\rm cm}^{-3}$), and is given by

$$M_{\rm O} = 10^8 {\rm F([O\,I])} D^2 \times \exp\left(\frac{2.28}{T_4}\right), \quad (4)$$

where $M_{\rm O}$ is the mass of neutral oxygen in $M_\odot$, F([O I]) is the flux of the [O I] λλ6300, 6363 peak in erg s^{-1}cm^{-2}, D is the distance in Mpc and T_4 is the temperature of the oxygen-emitting region of the spectrum in units of 10^4 K. The temperature of the [O I] region can be determined by the ratio of fluxes between [O I] 5577 Å and the [O I] λλ6300, 6363 lines. However, determining the flux of the [O I] 5577 Å peak is not easy, as it can blend with Fe II lines, distorting the flux value of the peak. As such, a temperature of $T_4 = 0.4$ K was used, which arises from the assumption that within the oxygen emitting region during the nebular phase the density is high and the temperature is low (Elmhamdi et al. 2004). Using this low temperature, along with an F([O I]) $= 8.41 \times 10^{-14}$ erg s^{-1} cm^{-2} derived from the spectrum taken at ∼170 d post-explosion, results in an oxygen mass of $M_{\rm O} = 3.13 \pm 0.07$ $M_\odot$. This is a large oxygen mass given the ejecta mass derived from the light curve. However, realistically, the flux of oxygen is not constant over time as the SN fades and the spectra transitions further into the nebular phase. As such, different oxygen masses can be obtained as the spectra evolve, the values of which are given in Table 5. Due to the changing nature of the oxygen flux as SN 2020acat fades, the value of $M_{\rm O}$ derived from the spectrum taken on day ∼171 can be considered an upper limit to the oxygen mass.

Two of the nebular spectra of SN 2020acat ($t = 171.17$ and $t = 233.63$) were modelled using our SN nebular spectrum synthesis code (e.g. Mazzali et al. 2007). Briefly, the code computes the emission of gamma rays and positrons by the radioactive decay of ^{56}Ni and ^{56}Co, and computes their deposition in the expanding SN ejecta, using a gamma-ray opacity $\kappa_{\rm gamma} = 0.027 {\rm g\,cm}^{-2}$ and a positron opacity $\kappa_{e^+} = 7\,{\rm g\,cm}^{-2}$. Following the prescriptions of Axelrod (1980), the deposited energy is utilized to heat the gas via collisional processes. Heating is then balanced by cooling via radiation in mostly forbidden lines. Ionization and recombination rates are balanced and the level populations within different ions is computed in non-local thermodynamic equilibrium (NLTE). The SN nebula is expected to be optically thin at late times and radiation transport is not performed. For SN 2020acat, we use a simple one-zone version of the code, which allows us to determine the basic parameters of the inner ejecta without making assumptions about the density distribution. Clearly, because of such an approach, our results must be regarded as approximate. We assumed for the two spectra at ∼231 and 170 d after explosion, used a distance modulus $\mu = 32.74$ mag and a total reddening $E(B-V) = 0.0207$ mag. The outer boundary velocity for the part of the nebula that contributes to the emission was set at 5100 km s^{-1}, based on the width of the

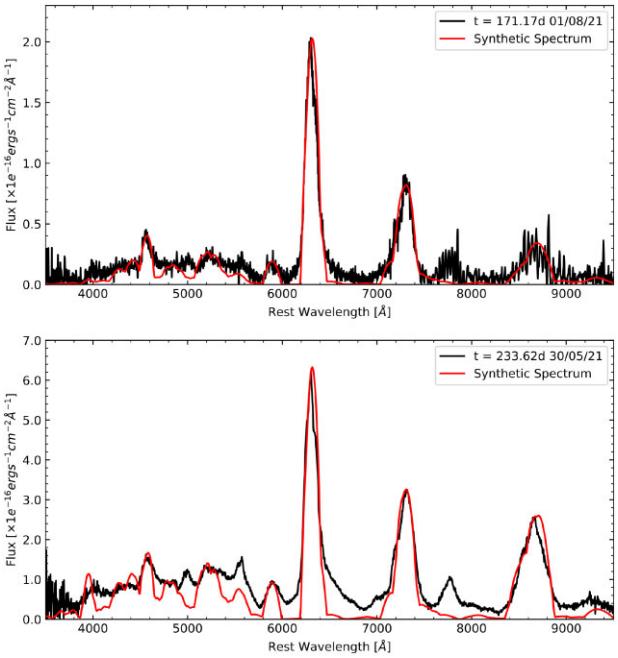

Figure 13. Nebular phase spectra (black) of SN 2020acat, taken at ∼171.17 (top panel) and 233.62 (bottom panel) d post-explosion, along with the one-zone nebular model (red) of Mazzali et al. (2001).

emission lines. Given that we did not use a stratified model of the ejecta, we should expect that deposition efficiency decreases with time faster than in the real SN. This means that at later epochs somewhat larger values of the masses are required to fit the spectrum (Mazzali et al. 2001). Fig. 13 shows the two observed spectra and the corresponding synthetic spectra. The main emission features are [O I] 6300,6363 Å, Mg I] 4570 Å, and Ca II] 7291,7324 Å. Weaker lines include [O I] 5577 Å, which is sensitive to recombination, the [O I] recombination line near 7773 Å, which is not reproduced in our model as we do not consider recombination emission, Na I D, and several [Fe II] lines, mostly near 5200 Å, which are important to determine the abundance of ^{56}Ni. The mean masses of the elements that contribute to the spectra are $^{56}{\rm Ni} = 0.10 \pm 0.02$, $M_{\rm O} = 1.0 \pm 0.10$, $M_{\rm C} = 0.20 \pm 0.05$, $M_{\rm Ca} = 0.045 \pm 0.005$, $M_{\rm Mg} = 0.0012 \pm 0.0004$, and $M_{\rm Na} = 0.0008 \pm 0.0001$ $M_\odot$. Small amounts of Si and S were also included for consistency, but these elements do not produce strong lines in the optical range. The spectra do not appear to be fully nebular. In particular, a feature near 5000 Å may still have a P-Cygni profile from Fe II multiplet 42 lines. The ejected mass within the boundary velocity is 1.5 ± 0.15 $M_\odot$. This indicates a moderately massive CO core (∼3 $M_\odot$ if we assume a neutron star remnant), and is consistent with previous results for stripped-envelope SNe (e.g. Mazzali et al. 2021, fig. 14), indicating a progenitor ZAMS mass of ∼20 $M_\odot$.

6 CONCLUSIONS

SN 2020acat was a well-observed SN IIb, with a highly constrained explosion date, that was thoroughly observed in the UV to NIR photometric regions during peak time, and extensive optical follow-up during the transition into the nebular phase. Spectroscopically, SN 2020acat was followed for ∼230 d, resulting in a comprehensive optical campaign from pre-maximum light to the start of the nebular phase. The follow-up campaign was unfortunately halted

as SN 2020acat moved into Solar conjunction and was too faint to be observed once it reappeared. The comprehensive photometric and spectroscopic data set gives SN 2020acat one of the best follow-up campaign available for an SN IIb caught within a few days of its explosion.

SN 2020acat displays a very fast rise, reaching the peak of the pseudo-bolometric light curve in ∼15 d, more rapidly than other SNe IIb. The fast rising pseudo-bolometric light curve, and the underestimation of the light-curve model used in Section 4.3, may result from ^{56}Ni being mixed into the outer layers of the ejecta releasing trapped photons at a much faster rate than the standard SNe IIb. However, more detailed modelling of the pseudo-bolometric light curve is required to determine the distribution of ^{56}Ni within the ejecta of SN 2020acat. Along with the fast rising pseudo-bolometric light curve SN 2020acat lacks any early time decline that is normally associated with the shock-cooling tail, which is also seen in its early time UV and optical light curves. While it might be possible that the shock-cooling phase was completely missed in the early time observations, the dim initial observation as well as the shape of the rising light curves and the tight constraint on the estimated explosion date, all suggest that SN 2020acat lacked any evident shock-cooling phase. The lack of an extended shock-cooling phase strongly implies that the progenitor of SN 2020acat was a compact object that lacked an extended hydrogen envelope.

Modelling of the pseudo-bolometric light curve showed that SN 2020acat produced a mass of ^{56}Ni of $M_{\rm Ni} = 0.13 \pm 0.03$ M$_\odot$ along with an ejecta mass of $M_{\rm ej} = 2.3 \pm 0.4$ M$_\odot$ and a kinetic energy of $E_{\rm k} = 1.2 \pm 0.3 \times 10^{51}$ erg. When compared to other SNe IIb, SN 2020acat was found to have synthesized a larger amount of ^{56}Ni, and produced a slightly larger ejecta mass and kinetic energy, implying that SN 2020acat originated from a more massive star than the average hydrogen-rich SE-SNe. From the derived physical parameters, assuming a remnant mass of ∼1.5–2.5 M$_\odot$, and using the set of progenitor models described in Sukhbold et al. (2016), a progenitor mass range of $M_{\rm ZAMS} \approx$ 15–20 M$_\odot$ was determined for SN 2020acat. This progenitor mass range agrees with the derived $M_{\rm ZAMS}$ obtained from analysis of the nebular phase spectra, which obtained an $M_{\rm ZAMS}$ of ∼20 M$_\odot$, which together suggest that SN 2020acat likely originated from a relatively massive star.

Spectroscopically, SN 2020acat shows strong hydrogen features throughout its evolution into the nebular phase, covering the first ∼100 d, at which point oxygen, along with calcium, starts to dominate the spectra. The clear presence of hydrogen well into the start of the nebular phase suggests that SN 2020acat possessed either a very dense thin hydrogen envelope prior to explosion or the hydrogen was mixed deep into the outer layers through some means of convection. In addition to the deep hydrogen signature within the spectra of SN 2020acat, the spectral feature usually associated with the Fe II λ5018 line was seen to be much stronger than the surrounding Fe II lines. From analysis of the spectra at multiple epochs around peak time, it was determined that the feature was likely enhanced by the presence of a combination of helium and nitrogen within the ejecta. While the helium line that could have enhanced this feature has been reported prior, the presence of nitrogen is not expected in the spectra of SNe IIb. One possible explanation for the origin of the nitrogen is if the progenitor of SN 2020acat was a massive enough star, then some nitrogen may still remain from the helium-burning stage and appears in the spectra as weak N II features. Future work on modelling the evolution of SN 2020acat is required to investigate the potential presence of nitrogen in its spectra at early epochs.

ACKNOWLEDGEMENTS

This work makes use of observations from the Las Cumbres Observatory network. The LCO team is supported by NSF grants AST-1911225 and AST-1911151, and NASA *SWIFT* grant 80NSSC19K1639. This paper is based in part on observations made with the Liverpool Telescope operated on the island of La Palma by Liverpool John Moores University in the Spanish Observatorio del Roque de los Muchachos of the Institutode Astrofisica de Canarias with financial support from the UK Science and Tech-nology Facilities Council. This work is partially based on observations collected at the Copernico 1.82-m and Schmidt 67/92 Telescopes operated by INAF Osservatorio Astronomico di Padova at Asiago, Italy. This paper is also based on observations made with the Nordic Optical Telescope, owned in collaboration by the University of Turku and Aarhus University, and operated jointly by Aarhus University, the University of Turku and the University of Oslo, representing Denmark, Finland, and Norway, the University of Iceland and Stockholm University at the Observatorio del Roque de los Muchachos, La Palma, Spain, of the Instituto de Astrofisica de Canarias. The data presented here were obtained in part with ALFOSC, which is provided by the Instituto de Astrofisica de Andalucia (IAA) under a joint agreement with the University of Copenhagen and NOT. This work is partly based on the NUTS2 programme carried out at the NOT. NUTS2 is funded in part by the Instrument Center for Danish Astrophysics (IDA). CA is supported by NASA grant 80NSSC19K1717 and NSF grants AST-1920392 and AST-1911074. TM-B acknowledges financial support from the Spanish Ministerio de Ciencia e Innovación (MCIN), the Agencia Estatal de Investigación (AEI) 10.13039/501100011033 under the PID2020-115253GA-I00 HOSTFLOWS project, and Centro Superior de Investigaciones Científicas (CSIC) under the PIE project 20215AT016. AR acknowledges support from ANID BECAS/DOCTORADO NACIONAL 21202412. LG acknowledges financial support from the Spanish Ministerio de Ciencia e Innovación (MCIN), the Agencia Estatal de Investigación (AEI) 10.13039/501100011033, and the European Social Fund (ESF) 'Investing in your future' under the 2019 Ramón y Cajal program RYC2019-027683-I and the PID2020-115253GA-I00 HOSTFLOWS project, and from Centro Superior de Investigaciones Científicas (CSIC) under the PIE project 20215AT016. IA is a CIFAR Azrieli Global Scholar in the Gravity and the Extreme Universe Program and acknowledges support from that program, from the European Research Council (ERC) under the European Union's Horizon 2020 research and innovation program (grant agreement number 852097), the Israel Science Foundation (grant number 2752/19), the United States-Israel Binational Science Foundation (BSF), and the Israeli Council for Higher Education Alon Fellowship. MG is supported by the EU Horizon 2020 research and innovation programme under grant agreement No. 101004719. MN is supported by the European Research Council (ERC) under the European Union's Horizon 2020 research and innovation programme (grant agreement No. 948381) and by a Fellowship from the Alan Turing Institute. NER acknowledges partial support from MIUR, PRIN 2017 (grant 20179ZF5KS), the Spanish MICINN grant PID2019-108709GB-I00 and FEDER funds, and the program Unidad de Excelencia María de Maeztu CEX2020-001058-M. TMR acknowledges the financial support of the Vilho, Yrjö and Kalle Väisälä Foundation of the Finnish Academy of Science and Letters. Y-ZC is funded by China Postdoctoral Science Foundation (grant no. 2021M691821). PL and ME acknowledge support from the Swedish Research Council. PC is supported by a research grant (19054) from VILLUM FONDEN.

DATA AVAILABILITY

Spectroscopic data will be made available on the Weizmann Interactive Supernova Data Repository (WISeREP; Yaron & Gal-Yam 2012) at https://wiserep.weizmann.ac.il/. Photometric data are available as supplementary data, and is organized by the telescope used to obtain the data. The files includes data from Asiago, ATLAS, LCO, LT, NOT, *Swift*, and ZTF.

REFERENCES

Arcavi I. et al., 2011, ApJ, 742, L18
Arcavi I. et al., 2017, ApJ, 837, L2
Arnett W. D., 1982, ApJ, 253, 785
Axelrod T. S., 1980, PhD thesis, Univ. California
Barbon R., Benetti S., Cappellaro E., Patat F., Turatto M., Iijima T., 1995, A&AS, 110, 513
Bellm E. C. et al., 2018, PASP, 131, 018002
Bersten M. C. et al., 2012, ApJ, 757, 31
Bersten M. C. et al., 2018, Nature, 554, 497
Brown P. J., Breeveld A. A., Holland S., Kuin P., Pritchard T., 2014, Ap&SS, 354, 89
Brown T. M. et al., 2013, PASP, 125, 1031
Buzzoni B. et al., 1984, The Messenger, 38, 9
Cutri R. M. et al., 2013, Explanatory Supplement to the AllWISE Data Release Products. Available at: ALLWISE Data Release
Deng J., Mazzali P., Maeda K., Nomoto K., 2003, Nucl. Phys. A, 718, 569
Dessart L., Hillier D. J., 2005, A&A, 439, 671
Dessart L., Hillier D. J., Woosley S., Livne E., Waldman R., Yoon S.-C., Langer N., 2016, MNRAS, 458, 1618
Djupvik A. A., Andersen J., 2010, in Diego J. M., Goicoechea L. J., González-Serrano J. I., Gorgas J., eds, Astrophys. Space Sci. Proc., Highlights of Spanish Astrophysics V. Springer-Verlag, Berlin, p. 211
Drake G., 2006, High Precision Calculations for Helium. Springer, New York, NY
Dyk S. D. V. et al., 2014, ApJ, 147, 37
Elmhamdi A., Danziger I. J., Cappellaro E., Della Valle M., Gouiffes C., Phillips M. M., Turatto M., 2004, A&A, 426, 963
Ergon M. et al., 2014, A&A, 562, A17
Filippenko A., 2000, AIP Conf. Proc. Vol. 522, Cosmic Explosions: Tenth Astrophysics Conference. Am. Inst. Phys., New York, p. 123
Folatelli G., Bersten M. C., Kuncarayakti H., Benvenuto O. G., Maeda K., Nomoto K., 2015, ApJ, 811, 147
Fransson C., Chevalier R. A., 1989, ApJ, 343, 323
Gilkis A., Arcavi I., 2022, MNRAS, 511, 691
Gräfener G., Vink J. S., 2015, MNRAS, 455, 112
Hachinger S., Mazzali P. A., Taubenberger S., Hillebrandt W., Nomoto K., Sauer D. N., 2012, MNRAS, 422, 70
Hamuy M. et al., 2001, ApJ, 558, 615
Howell D., 2019, Am. Astron. Soc. Meeting Abstr. 233, 258.16
Jerkstrand A., Ergon M., Smartt S. J., Fransson C., Sollerman J., Taubenberger S., Bersten M., Spyromilio J., 2015, A&A, 573, A12
Jordi K., Grebel E. K., Ammon K., 2006, A&A, 460, 339
Khatami D. K., Kasen D. N., 2019, ApJ, 878, 56
Kumar B. et al., 2013, MNRAS, 431, 308
Lantz B. et al., 2004, in Mazuray L., Rogers P. J., Wartmann R., eds, Proc. SPIE Conf. Ser. Vol. 5249, Optical Design and Engineering. SPIE, Bellingham, p. 146
Lewis J. R. et al., 1994, MNRAS, 266, L27
Luo D., Pradhan A. K., 1989, J. Phys. B: At. Mol. Opt. Phys, 22, 3377
Lyman J. D., Bersier D., James P. A., Mazzali P. A., Eldridge J. J., Fraser M., Pian E., 2016, MNRAS, 457, 328
Malesani D. et al., 2009, ApJ, 692, L84
Marion G. H. et al., 2014, ApJ, 781, 69
Mazzali P. A., Nomoto K., Patat F., Maeda K., 2001, ApJ, 559, 1047
Mazzali P. A. et al., 2005, Science, 308, 1284
Mazzali P. A. et al., 2007, ApJ, 670, 592
Mazzali P. A., Pian E., Bufano F., Ashall C., 2021, MNRAS, 505, 4106
Moorwood A., Cuby J. G., Lidman C., 1998, The Messenger, 91, 9
Morales-Garoffolo A. et al., 2014, MNRAS, 445, 1647
Morales-Garoffolo A. et al., 2015, MNRAS, 454, 95
Mould J. R. et al., 2000, ApJ, 529, 786
Naiman B. V., Sabach E., Gilkis A., Soker N., 2019, MNRAS, 491, 2736
O'Connor E., Ott C. D., 2011, ApJ, 730, 70
Pastorello A. et al., 2008, MNRAS, 389, 955
Pessi P. et al., 2020, Transient Name Server AstroNote, 248, 1
Pessi P. J. et al., 2019, MNRAS, 488, 4239
Piascik A. S., Steele I. A., Bates S. D., Mottram C. J., Smith R. J., Barnsley R. M., Bolton B., 2014, in Ramsay S. K., McLean I. S., Takami H., eds, Proc. SPIE Conf. Ser. Vol. 9147, Ground-based and Airborne Instrumentation for Astronomy V. SPIE, Bellingham, p. 2703
Podsiadlowski P., Joss P. C., Hsu J. J. L., 1992, ApJ, 391, 246
Prentice S. J. et al., 2016, MNRAS, 458, 2973
Prentice S. J. et al., 2019, MNRAS, 485, 1559
Richmond M. W., Treffers R. R., Filippenko A. V., Paik Y., Leibundgut B., Schulman E., Cox C. V., 1994, AJ, 107, 1022
Richmond M. W., Treffers R. R., Filippenko A. V., Paik Y., 1996, AJ, 112, 732
Roming P. W. A. et al., 2005, Space Sci. Rev., 120, 95
Roming P. W. A. et al., 2009, ApJ, 704, L118
Sahu D. K., Anupama G. C., Chakradhari N. K., 2013, MNRAS, 433, 2
Sana H. et al., 2012, Science, 337, 444
Schlafly E. F., Finkbeiner D. P., 2011, ApJ, 737, 103
Smartt S. J., 2009, ARA&A, 47, 63
Smartt S. J. et al., 2015, A&A, 579, A40
Smith K. W. et al., 2020, PASP, 132, 085002
Smith N., Li W., Filippenko A. V., Chornock R., 2011, MNRAS, 412, 1522
Spergel D. N. et al., 2007, ApJS, 170, 377
Sravan N., Marchant P., Kalogera V., 2019, ApJ, 885, 130
Srivastav S. et al., 2020, Transient Name Server AstroNote, 249, 1
Steele I. A. et al., 2004, in Oschmann J. M., Jr, ed., Proc. SPIE Conf. Ser. Vol. 5489, Ground-based Telescopes. SPIE, Bellingham, p. 679
Sukhbold T., Ertl T., Woosley S. E., Brown J. M., Janka H. T., 2016, ApJ, 821, 38
Tachiev G., Fischer C. F., 2001, Can. J. Phys., 79, 955
Taddia F. et al., 2018, A&A, 609, A136
Takáts K., Vinkó J., 2012, MNRAS, 419, 2783
Taubenberger S. et al., 2011, MNRAS, 413, 2140
Tonry J. L. et al., 2018, PASP, 130, 064505
Tsvetkov D. Y., Volkov I. M., Baklanov P., Blinnikov S., Tuchin O., 2009, Perem. Zvezdy, 29, 2
Tsvetkov D. Y., Volkov I. M., Sorokina E. I., Blinnikov S. I., Pavlyuk N. N., Borisov G. V., 2012, Perem. Zvezdy, 32, 6
Uomoto A., 1986, ApJ, 310, L35
Wheeler J. C. et al., 1993, ApJ, 417, L71
Wheeler J. C., Johnson V., Clocchiatti A., 2015, MNRAS, 450, 1295
Wilson R. N., 1983, in Swings J. P., Kjaer K., eds, European Southern Observatory Conference and Workshop Proceedings, Vol. 17, European Southern Observatory, Garching, p. 173
Woosley S. E., Eastman R. G., Weaver T. A., Pinto P. A., 1994, ApJ, 429, 300
Woosley S. E., Sukhbold T., Kasen D. N., 2021, ApJ, 913, 145
Yaron O., Gal-Yam A., 2012, PASP, 124, 668
Yoon S.-C., Dessart L., Clocchiatti A., 2017, ApJ, 840, 10
Zapartas E. et al., 2021, A&A, 656, L19

SUPPORTING INFORMATION

Supplementary data are available at *MNRAS* online.

NIR_bands.txt
Optical_bands.txt
UV_bands.txt

Please note: Oxford University Press is not responsible for the content or functionality of any supporting materials supplied by the authors. Any queries (other than missing material) should be directed to the corresponding author for the article.

[1]*Astrophysical Research Institute Liverpool John Moores University, Liverpool L3 5RF, UK*
[2]*Max-Planck Institute for Astrophysics, Karl-Schwarzschild-Str. 1, D-85748 Garching, Germany*
[3]*Institute for Astronomy, University of Hawai'i at Manoa, 2680 Woodlawn Dr., Hawai'i, HI 96822, USA*
[4]*European Southern Observatory, Alonso de Córdova 3107, Casilla 19, Santiago, Chile*
[5]*The School of Physics and Astronomy, Tel Aviv University, Tel Aviv 69978, Israel*
[6]*CIFAR Azrieli Global Scholars program, CIFAR, Toronto, ON M5G 1M1, Canada*
[7]*INAF – Osservatorio Astronomico di Padova, Vicolo dell'Osservatorio 5, I-35122 Padova, Italy*
[8]*DIRAC Institute, Department of Astronomy, University of Washington, 3910 15th Avenue NE, Seattle, WA 98195, USA*
[9]*Las Cumbres Observatory, 6740 Cortona Dr, Suite 102, Goleta, CA 93117-5575, USA*
[10]*Department of Physics, University of California, Santa Barbara, CA 93106-9530, USA*
[11]*Physics Department and Tsinghua Center for Astrophysics (THCA), Tsinghua University, Beijing 100084, China*
[12]*DTU Space, National Space Institute, Technical University of Denmark, Elektrovej 327, DK-2800 Kgs. Lyngby, Denmark*
[13]*Institute of Space Sciences (ICE, CSIC), Campus UAB, Carrer de Can Magrans s/n, E-08193 Barcelona, Spain*
[14]*Department of Astronomy, AlbaNova University Center, Stockholm University, SE-10691 Stockholm, Sweden*
[15]*The Oskar Klein Centre, AlbaNova, SE-10691 Stockholm, Sweden*
[16]*Institut d'Estudis Espacials de Catalunya (IEEC), E-08034 Barcelona, Spain*
[17]*Astronomical Observatory, University of Warsaw, Al. Ujazdowskie 4, PL-00-478 Warszawa, Poland*
[18]*Center for Astrophysics | Harvard & Smithsonian, 60 Garden Street, Cambridge, MA 02138-1516, USA*
[19]*The NSF AI Institute for Artificial Intelligence and Fundamental Interactions, 77 Massachusetts Ave, 26-555. Cambridge, MA 02139, USA*
[20]*Cardiff Hub for Astrophysics Research and Technology, School of Physics and Astronomy, Cardiff University, Queens Buildings, The Parade, Cardiff CF24 3AA, UK*
[21]*Birmingham Institute for Gravitational Wave Astronomy and School of Physics and Astronomy, University of Birmingham, Birmingham B15 2TT, UK*
[22]*IAASARS, Observatory of Athens, 15236 Penteli, Greece*
[23]*Nordic Optical Telescope, Apartado 474, 38700 Santa Cruz de La Palma, Santa Cruz de Tenerife, Spain*
[24]*Facultad de Ciencias Astronómicas y Geofísicas, Universidad Nacional de La Plata, Paseo del Bosque S/N, B1900FWA La Plata, Argentina*
[25]*Departamento de Ciencias Físicas – Universidad Andres Bello, Avda. República 252, Santiago, Chile*
[26]*Millennium Institute of Astrophysics, Nuncio Monsenor Sótero Sanz 100, Providencia, Santiago, Chile*
[27]*The Cosmic Dawn Center (DAWN), Niels Bohr Institute, University of Copenhagen, Rådmandsgade 62, DK-2200 København N, Denmark*
[28]*Inter-University Centre for Astronomy and Astrophysics, Pune 411007, India*
[29]*Astrophysics Research Centre, School of Mathematics and Physics, Queen's University Belfast, Belfast BT7 1NN, UK*

This paper has been typeset from a TEX/LATEX file prepared by the author.